

Chirality and Rashba-related Effects in the Spin Texture of a Two-Dimensional Centro-Symmetric Ferromagnet: the Case of CrI₃ Bilayer

Sukanya Ghosh,^{*} Nataša Stojić, and Nadia Binggeli
Abdus Salam International Centre for Theoretical Physics, Trieste, Italy[†]
(Dated: December 2018)

I. ABSTRACT

The newly discovered two-dimensional (2D) magnetic semiconductors such as CrI₃ have triggered a surge of interest stemming from their exotic spin-dependent properties and potential applications in spintronics and magneto-optoelectronics. Using first-principle density-functional-theory calculations, we investigate the properties of the spin-polarization texture in momentum space in the prototype 2D centrosymmetric ferromagnetic (FM) bilayer of CrI₃, with perpendicular magnetization. The FM bilayer displays a rich in-plane spin texture in its highest valence bands. We show the existence of two distinct spin canting effects, which result from the coupling of FM order with structural chirality and electric polarization, in establishing the in-plane spin texture. The first effect is generated by the chirality of the layer stacking and the spin-orbit-polarized nature of the valence states, and yields the same canting on both layers. The second effect is a Rashba-related effect, which in a centrosymmetric ferromagnet induces in a single electronic state two opposite spin-canted components on the two layers. Furthermore, using the FM bilayer as an example, we provide some general rules for centrosymmetric systems imposed by magnetic-space-group symmetries on spin-polarization vectors, serving as guidelines for the shape of the spin texture in the Brillouin zone of such magnetic crystals. Finally, we show that the above effects can be effectively used to manipulate the spin texture via compressive strain, which induces in the FM bilayer valence-band-edge states with canted spins.

II. INTRODUCTION

Spin-orbit-coupled crystalline materials offer a fruitful ground for the observation of a variety of spin-related phenomena and opportunities for controlling spin-dependent properties by non-magnetic means via spin-orbit coupling (SOC).[1–3] One of such properties of relevance for spintronics is the spin texture of electronic bands in momentum space, as it determines how spin-polarized currents may be manipulated for spintronic devices.

Spin polarization in nonmagnetic materials has been traditionally ascribed to SOC in the presence of broken global inversion symmetry. The properties of the resulting non-trivial spin textures in momentum space have been widely studied for various classes of three-dimensional (3D) and two-dimensional (2D) non-magnetic crystalline systems lacking inversion symmetry.[4–14] This includes, in particular, crystal surfaces and interfaces, where SOC effects are enhanced by reduced dimensionality.[2] Furthermore, for nonmagnetic materials, general rules have been established, which provide simple symmetry-based guidelines on the shape of spin textures in the Brillouin zone (BZ).[14] In recent years, the discovery of hidden spin polarization[15, 16] and spin-layer locking[17] in inversion-symmetric non-magnetic semiconductors and semimetals has steered research interest towards centrosymmetric materials. This recent development has also shown that specific local-site inversion asymmetry combined with SOC could produce remarkable spin-polarization effects in the spin textures of nonmagnetic centrosymmetric crystals.[15–17]

In the past few years, an exciting new class of materials, the 2D magnetic materials, has been discovered.[18, 19] These materials are attracting enormous attention due to their peculiar spin-related phenomena and vast potential for magneto-optics, magneto-electronics, and spintronic devices.[20–22] This new class of materials belongs to the fast growing family of 2D van der Waals (vdW) materials, whose heterostructures hold great promises for nanoscale devices. Many of the 2D magnetic materials are semiconductors with centrosymmetric atomic geometries, e.g., CrI₃, CrBr₃, CrCl₃, Cr₂Ge₂Te₆, and show ferromagnetism or layer-dependent ferromagnetism.[18, 19, 23, 24] Importantly, the magnetism in such ultrathin magnetic materials can be tailored by external perturbations such as electric field,[25, 26] pressure,[27, 28] doping,[29–31] and stacking engineering.[23, 27, 28]

The emergence of the 2D magnetic semiconductors is opening the door to the design and fabrication of novel vdW spintronic, [32–36] magneto-optical[37] and magneto-(opto)electronic[38, 39] devices. In view of the incorporation of 2D magnetic materials in vdW devices it is important to know and understand the properties of their band-spin texture and the mechanisms that control them—in order also to manipulate them. General symmetry-based rules serving as guidelines on the shape of spin textures in the BZ of magnetic materials would also be helpful. So far, however, the band-spin textures in momentum space of magnetic materials with inherent SOC, and in particular of ferromagnets, have remained

^{*} Presently address : Materials Theory Division, Department of Physics and Astronomy, Uppsala University, 75120 Uppsala, Sweden

[†] email : sukanya.ghosh@physics.uu.se

largely unexplored. Only recently have a few investigations started to examine magnetic-order effects on the spin texture of some antiferromagnets,[40–43] while other studies have focused on surface/interface states and indicated Rashba effects and helical spin texture at ferromagnet surfaces/interfaces.[44–46]

Here we explore the properties of the band-spin texture in momentum space for a ferromagnetic (FM) vdW bilayer of CrI_3 , based on first-principles calculations. This system exemplifies the effects of chirality and electric polarization combined with FM order in establishing the spin-texture features of a relativistic centrosymmetric magnet. CrI_3 is a particularly interesting example of 2D vdW magnetic semiconductors, with perpendicular magnetization easy axis. The CrI_3 monolayer is FM, whereas the CrI_3 bilayer in its most common experimental form is a layered antiferromagnet,[25, 47] with a weak interlayer exchange coupling. This makes possible switching experimentally from the AFM to the FM phase with low magnetic field,[19] and most remarkably also by electrical means, such as electrostatic doping and electric field.[25, 29] Change in the layer stacking was also shown to change the magnetic coupling from AFM to FM.[28, 48–50] CrI_3 possesses rather strong Cr magnetic moments oriented perpendicular to the layers and a hefty Iodine SOC.[51] Earlier studies of the bilayer and monolayer have shown that SOC has a major impact on the highest valence states, while the lowest conduction bands remain essentially unaffected by relativistic effects.[51, 52]

In this work we examine the spin texture for the highest valence states of the CrI_3 FM bilayer, and compare to the FM monolayer and AFM bilayer.[43] In contrast to the latter cases, the FM bilayer displays a rich in-plane spin texture for the highest valence band. It includes alternating radial-spin features and vortices which are induced around the BZ center by the interlayer interaction. We identify the mechanisms leading to such features and their specific chiral origins. We also investigate the canting of the spin-polarization vectors on each of the CrI_3 monolayers, and disclose an interesting Rashba-related frustration effect present in such centrosymmetric ferromagnets. Using the FM bilayer as an example, we determine general rules imposed on spin textures by magnetic-group symmetries. We show that symmetry operators that combine time reversal with rotations and reflections in magnetic groups of centrosymmetric systems give rise to rules for the spin texture in the BZ which are reversed with respect to those established for non-magnetic groups —i.e., they impose that spin-polarization vectors are parallel to mirror planes and perpendicular to rotation axes for such operators. Finally, we show for the CrI_3 FM bilayer that vertical compressive strain can be used to effectively manipulate the spin texture and induce valence-band-edge states with canted spin polarization.

The remainder of this paper is organized as follows: in the next section the main structural and magnetic properties of the bilayer and monolayer CrI_3 are described, which is followed by the account of methods and pa-

rameters of calculations. The results part of the paper starts with the presentation of the spin texture of the highest valence state on the FM CrI_3 -bilayer in k -space in Section V, while the layer dependence of the spin-polarization density is presented in Section VI. The effect of the FM symmetries on the spin texture is presented in the subsequent section, and the two mechanisms responsible for the formation of the bilayer spin texture, namely the interactions through the local electric field (Rashba effect) and through the interlayer chiral potentials, are explained in Section VIII. After that, in Section IX, we show how the spin texture can be manipulated and the summary of the main results is given in Conclusions. The appendix contains information on the monolayer spin texture and band structure, the spin texture of the second valence state of the bilayer and explains further the calculation of the Rashba and chiral-interaction terms.

III. SYSTEM AND SYMMETRIES: BILAYER VERSUS MONOLAYER

In this study we focus mainly on the CrI_3 FM bilayer with monoclinic layer stacking, displayed in Fig. 1. In each of the CrI_3 monolayers, shown in this figure, the plane of Cr^{3+} ions is sandwiched between two planes of I^- ions, and the Cr^{3+} ions form a honeycomb lattice. Each Cr^{3+} ion has six nearest-neighbor I^- ions (three from the upper I plane and three from the lower I plane) forming a network of edge-sharing iodine octahedra. The spin magnetic moment per Cr is $3\mu_B$.

The CrI_3 bilayer is observed experimentally in two different structural phases which differ in their van-der-Waals CrI_3 -layer stacking, i.e., monoclinic versus rhombohedral stacking. They correspond to the stacking configurations present in the bulk- CrI_3 high-temperature (monoclinic) and low-temperature (rhombohedral) phases, respectively. Bulk CrI_3 has as stable phase the rhombohedral structure (with $R\bar{3}$ space group) below ~ 200 K, and the monoclinic structure (C_{2h} space group) at higher temperatures.[53]

The bilayer with monoclinic stacking (C_{2h} symmetry) is the common form obtained by exfoliation from bulk CrI_3 at room temperature, and remains experimentally in that structure when cooled to low temperatures.[47, 54] The bilayer in that structure has been the focus of most attention due to its layered antiferromagnetic (AFM) ground state (below $T_N \approx 45$ K), which can be conveniently switched to the FM state (by electric or magnetic means).[19, 25, 29] The bilayer with rhombohedral stacking (S_6 symmetry) is obtained experimentally by layer-stacking engineering, and is FM.[27, 28] Although in this paper we mainly focus on the spin texture of the FM bilayer with monoclinic stacking, we will also show that virtually the same spin texture pattern is present in the FM bilayer with rhombohedral stacking.

The two experimental structures of the bilayer correspond to configurations in which the two CrI_3 monolay-

ers have the same chirality,[55] as identified by the directions of the triangles corresponding to the top facets of the iodine octahedra (see solid triangles in Fig. 1(b)) —or equivalently by the upward oriented directions of the body diagonals of the octahedra (see blue arrows in Fig. 1(a) and (b)). Other meta-stable closed-packed structures of the CrI_3 bilayer have been predicted theoretically, and include structures in which the two layers have opposite chirality.[55] The later structures were shown to be FM.[55]

Unlike the two experimental structures, the non-chiral bilayer structures[55] are characterized by a horizontal mirror-reflection plane, M_{xy} , which transforms the bilayer into itself or a translation of itself. In the following we define as “chiral” structures, the atomic geometries lacking such symmetry (which include the two experimental forms of the bilayer as well as the monolayer). We note that we use this definition strictly in the context of FM crystals with perpendicular magnetization considered in this work. In that case, for a given chosen spin magnetization orientation \hat{z} , e.g., upward in Fig. 1(a), the chiral bilayer or monolayer structure and its horizontal mirror reflection are non-superposable (as left-handed and right-handed) configurations.

There are three particular directions related to the structural chirality of the bilayer (and of the monolayer), which correspond to the oriented diagonals of the Iodine octahedra (with directions pointing from bottom to top I-layer atom) —one of these directions is the z' axis indicated in Fig. 1(a). These three directions have the same tilt angle ($\theta = 55.4^\circ$) with respect to the vertical z axis and are enclosed in three vertical planes rotated by 120° from each other about the z axis. The projections of these three directions on the horizontal xy plane are indicated (blue arrows) in Fig. 1(b).

The CrI_3 single monolayer is FM below $T_C = 45$ K (with D_{3d} atomic-structure symmetry). The relativistic band structures of the FM monolayer and bilayers have been reported in previous studies.[43, 49, 51, 52] The CrI_3 monolayer exhibits an upper valence band which is isolated in energy over almost the whole BZ —except at the BZ-edge K point (see Appendix). This band has a spin polarization which is virtually parallel to the Cr spin moments,[43] except near the BZ edge, and displays thus a negligible in-plane spin texture in the main central part of the BZ (see Appendix). In the bilayer, on the contrary, as will be shown in this study, the upper valence band displays an interesting and intense in-plane spin texture. This makes the CrI_3 bilayer a convenient system to study the effects of interlayer interactions on the spin texture of a vdW FM bilayer. In the following, unless otherwise mentioned, the results shown are for the CrI_3 FM bilayer with monoclinic stacking.

The magnetic point group of the FM bilayer with monoclinic stacking is $C_{2h}[C_i]$ and corresponds to the symmetry operations: i) identity E, ii) inversion I, iii) 180° rotation about the y axis combined with time reversal $R_y[180^\circ]\cdot T$, and iv) xz mirror-plane reflection combined with time reversal $M_{xz}\cdot T$. The magnetic point group of

the single FM monolayer is $D_{3d}[S_6]$, while that of the FM bilayer with rhombohedral stacking is just S_6 .

IV. COMPUTATIONAL METHODS

Our calculations are performed using density functional theory (DFT) as implemented in the Quantum ESPRESSO package with a plane-wave basis set.[56] The exchange-correlation interactions between electrons are treated within the local spin density approximations (LSDA).[57, 58] Spin-orbit coupling is included within the (non-collinear) spinor DFT formalism using fully-relativistic projector-augmented-wave (PAW) pseudopotentials.[59, 60] The plane-wave kinetic energy cutoffs for the electronic orbitals and charge density are chosen to be 60 Ry and 650 Ry, respectively. The BZ is sampled using the uniform Monkhorst-Pack k -point grid of $24 \times 24 \times 1$. The periodic images of the CrI_3 bilayer are separated by a vacuum distance of ~ 30 Å along the out-of-plane direction (same for the monolayer). During structural relaxations atomic coordinates are relaxed until the forces on atoms become less than 1×10^{-4} Ry/Bohr.

The calculated in-plane lattice constant of the CrI_3 bilayer is $a = 6.69$ Å, while the equilibrium distance d (d_{int}) between the two outermost (innermost) iodine atomic layers of the bilayer is $d = 9.47$ Å ($d_{\text{int}}^{\text{eq}} = 3.36$ Å), consistent with previous LDA calculations.[51, 61] Within each CrI_3 monolayer, the vertical distance between the Cr plane and the innermost I layer (d_1) and outermost I layer (d_2) differ slightly (by $\sim 0.1\%$) in the bilayer configuration ($d_1 < d_2$), breaking the local inversion symmetry within each monolayer, while for the monolayer $d_1 = d_2$.

For the strained bilayer, we apply a vertical compressive strain $\epsilon_{zz} = -5\%$, as described in Ref.51. The optimized geometry is obtained by fixing the z coordinates of the outermost I atomic planes to the distance d contracted by 5%, while all other atomic coordinates are free to relax, and the in-plane lattice parameter is also optimized. The 5% compression expands the in-plane lattice parameter by 1% and reduces d_{int} by 9%. The magnetic anisotropy energies of the pristine and strained bilayer are found to be 0.65 meV/Cr and 0.36 meV/Cr, respectively,[51] establishing the fact that out-of-plane orientation of the Cr spin is favored in both cases.

We determine the spin texture of the bands in k -space by calculating the expectation values of the spin operators $\frac{1}{2}\hat{\sigma}_\alpha$, $\alpha = x, y, z$, in the Bloch spinor eigenfunctions $\Psi_{n,\mathbf{k}}(\mathbf{r})$:

$$S_\alpha(n, \mathbf{k}) = \frac{1}{2} \frac{\langle \Psi_{n,\mathbf{k}} | \hat{\sigma}_\alpha | \Psi_{n,\mathbf{k}} \rangle}{\langle \Psi_{n,\mathbf{k}} | \Psi_{n,\mathbf{k}} \rangle}, \quad (1)$$

where n is the band index and $\hat{\sigma}_x$, $\hat{\sigma}_y$, and $\hat{\sigma}_z$ are the Pauli matrices. To present the in-plane spin texture of the band, we display the spin-polarization vector $\mathbf{S}_\parallel(\mathbf{k}) = (S_x(\mathbf{k}), S_y(\mathbf{k}))$ at k -grid points of the 2D Brillouin zone (BZ), and for the out-of-plane spin texture, we show the map of S_z isovalues in the 2D BZ.

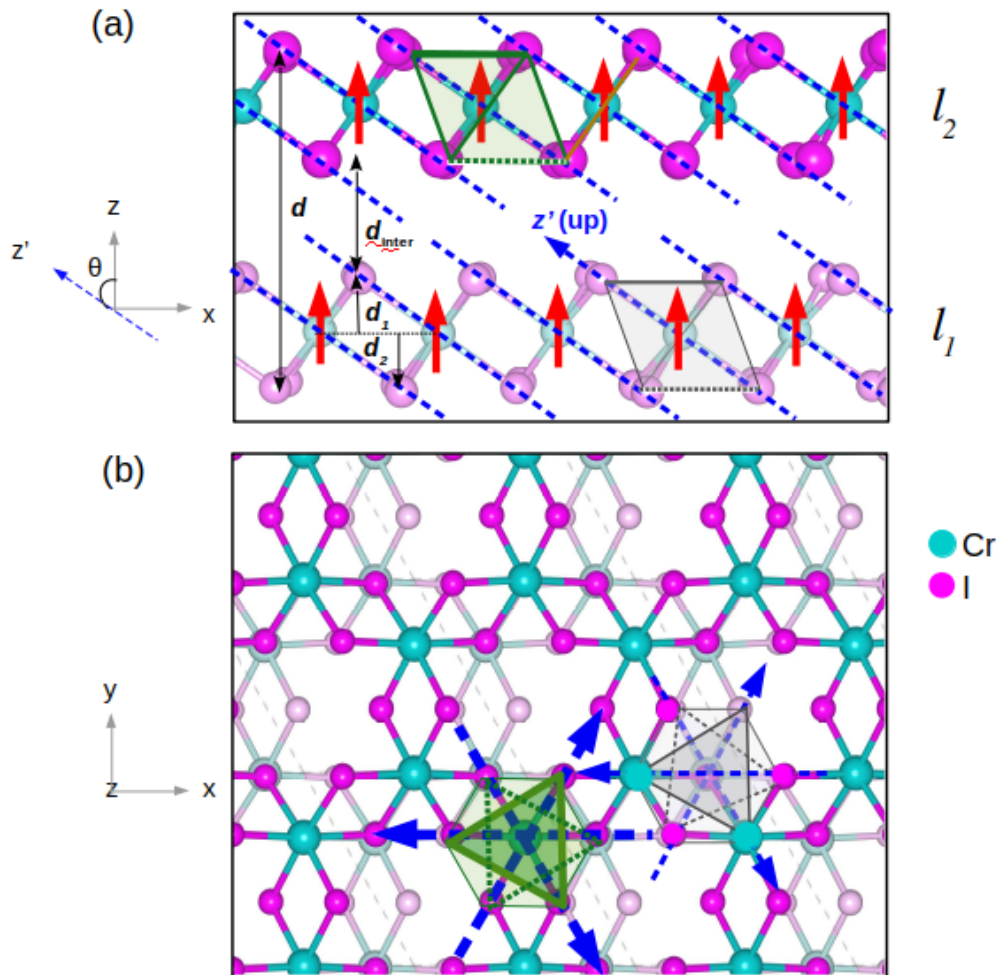


FIG. 1. Side view (a) and top view (b) of the CrI_3 FM bilayer with monoclinic layer stacking. The top (bottom) CrI_3 layer is indicated with bright (light) colors. The red arrows show the directions of the Cr spin moments. Each Cr atom is surrounded by six nearest neighbour I atoms, forming an octahedron, as indicated in green (grey) for the top (bottom) CrI_3 layer. The upper (lower) facet of the octahedron is shown by the solid (dotted) triangle. Dashed blue lines in (a) show the body diagonals of the iodine octahedra enclosed in planes parallel to the xz plane; these diagonals are aligned along the z' axis. The blue arrows in (b) show the projections of the directions of the body diagonals of octahedra oriented from bottom to top I-layer atoms. The thin black arrow in (a) shows the distance d_1 (d_2) in a CrI_3 monolayer between the Cr atomic plane and the I innermost (outermost) plane of the bilayer. The distance between the outermost (innermost) I planes of the bilayer d (d_{int}) is also shown.

For some specific $\Psi_{n,\mathbf{k}}$ states, we also examine the corresponding $\Psi_{n,\mathbf{k}}$ -state spin-polarization density, $\mathbf{m}^{(n,\mathbf{k})}(\mathbf{r})$, whose components are calculated as:

$$m_\alpha^{(n,\mathbf{k})}(\mathbf{r}) = \mu_B \Psi_{n,\mathbf{k}}^+(\mathbf{r}) \hat{\sigma}_\alpha \Psi_{n,\mathbf{k}}(\mathbf{r}), \quad (2)$$

where μ_B is the Bohr magneton.

We note that for centro-symmetric ferromagnets, although time reversal symmetry is broken, space-inversion symmetry still commutes with the Kohn-Sham Hamiltonian, H_{KS} . For the eigenvalues this implies: $E_n(-\mathbf{k}) = E_n(\mathbf{k})$, while for the non-degenerate eigenstates at \mathbf{k} (the typical case in a ferromagnet) this implies: $\mathbf{m}^{(n,-\mathbf{k})}(\mathbf{r}) = \mathbf{m}^{(n,\mathbf{k})}(-\mathbf{r})$ and $\mathbf{S}(n, -\mathbf{k}) = \mathbf{S}(n, \mathbf{k})$.

V. SPIN TEXTURE IN PRISTINE FM BILAYER

In Fig. 2, we display the in-plane spin texture for the highest valence band of the FM bilayer (with monoclinic stacking) in the 2D BZ. The energy-isovalued map of the band in k -space is also shown in this figure, for easy reference—with the valence band maximum (VBM) at Γ clearly visible. Contrary to the FM monolayer, whose in-plane spin texture is minute for the upper valence band (Fig. A1 in Appendix), for the bilayer the highest valence band displays significant spin canting away from the z axis, giving rise to a pronounced and interesting in-plane spin texture in the central part of the BZ.

The in-plane texture, in Fig. 2, has as dominant fea-

tures six intense “spin patches”, each made of strong parallel spins. These patches are located around Γ , along the $\Gamma - K'$, $\Gamma - K$, and equivalent directions, and have alternating inward and outward radial-spin directions. The patches do not correspond to any particular points in the band’s dispersion. One can notice, in between patches, around Γ , six alternate vortex structures with centers located at slightly larger distance from the BZ center, along the $\Gamma - M'$, $\Gamma - M$, and equivalent directions. All of these features are absent for the highest valence band of the monolayer, which exhibits a noticeable (but small) in-plane texture essentially only along the edge of the BZ, near the M point (Fig. A1). Although a similar BZ-edge spin pattern is also present for the highest valence band of the bilayer (with a slightly decreased intensity), it is barely visible on the scale of the bilayer spin texture in Fig. 2.

Proceeding thus from the monolayer to the bilayer causes intense in-plane spin patch features to appear in the spin texture of the highest valence band around Γ . We note that these spin-texture features are not connected to any structural relaxation of the monolayer due to the bilayer formation from isolated monolayers. This has been verified by constructing a bilayer with the same frozen monolayer Cr-I inter-planar distances as in the isolated monolayer, which gives a spin texture (see SI) virtually identical to that in Fig. 2. Hence, this indicates that the spin patches, in Fig. 2, are a direct effect of the interaction between the two monolayers on the electronic spin texture, which is a rather intriguing effect.

In addition, we find that when the interlayer stacking is changed from the monoclinic stacking (C_{2h}) to the rhombohedral stacking (S_6), which corresponds to the other experimentally known phase of the bilayer, almost the same in-plane spin texture is obtained for the upper valence band (see SI). Thus, the different relative-lateral translation of the CrI_3 monolayers, which differentiate the two structural phases, has only a minor influence on the in-plane spin texture. In fact, for the rhombohedral stacking, both the intensity of the in-plane spin texture $|\mathbf{S}_{\parallel}(\mathbf{k})|$ and the band energy $E(\mathbf{k})$ exhibit perfect hexagonal symmetry in the BZ, while for the monoclinic stacking, one can observe in the central part of the BZ, in Fig. 2, a slight uniaxial elongation along the k_y relative to k_x axis of both the spin-texture pattern and band-energy map. Such a smooth uniaxial deformation is a direct consequence of the monoclinic stacking characterized by a 2D macroscopic uniaxial anisotropy of the crystal structure along the y relative to x axis in the bilayer [see Fig. 1(b)].

For the states of the highest valence band, the maxima in the amplitude of $\mathbf{S}_{\parallel}(\mathbf{k})$ correspond to the six spin patches. The largest amplitude is obtained for the patches along the k_x axis, at $k_x = \pm 0.23 \cdot 2\pi/a$, and is 0.065. The amplitude of $\mathbf{S}_{\parallel}(\mathbf{k})$ is vanishing at the Γ point, at the centers of the vortices, and at the K and K' corners of the BZ. In Fig. 3, we show the values of the out-of-plane spin component S_z of the upper valence band in the 2D BZ. Similar to the layer-resolved spin

texture of the CrI_3 AFM bilayer,[43] a ring-type texture is observed in the S_z of the FM bilayer. In Fig. 3 the largest value is at the BZ centre and is 0.50; S_z decreases then with increasing k radius, reaching a minimum value of 0.43 at $k_x = \pm 0.3 \cdot 2\pi/a$. For larger radii, S_z smoothly increases with increasing radius up to the BZ edge, where it exhibits local maxima at K , K' , M , and M' . At the points where $|\mathbf{S}_{\parallel}|$ is the largest, its value is 15% of the amplitude of the out-of-plane spin component. We note that the vanishing in-plane spin components at Γ and at K , K' points correspond to the maximum and local maxima of S_z , respectively.

Similar to the highest valence band, we find that the second highest valence band also has the strongest $\mathbf{S}_{\parallel}(\mathbf{k})$ components located in spin-patch regions centered along the $\Gamma - K$ and $\Gamma - K'$ directions (see Fig. A3 in Appendix). For the second-highest valence band, however, the $\mathbf{S}_{\parallel}(\mathbf{k})$ components in the patches are aligned along the opposite direction in k -space with respect to those of the highest valence band, and there is no vortex. The spin patterns along the BZ edge (and in particular near M and M') are similar, instead, for the two bands, and have the same spin orientation, while the absence of vortices allows much larger values of the in-plane spins, close to the M' points. This BZ-edge pattern is a feature originating from the spin texture of the monolayer highest-valence band (see Fig. A1), which persists upon formation of the bilayer in the spin textures of its upper two valence bands.

For the $\mathbf{S}_{\parallel}(\mathbf{k})$ of the highest valence band, in Fig. 2, we note that the direction of the pre-existing (monolayer) BZ-edge spins along the $K - K'$ line and the directions of the spins in the patches along the $K' - \Gamma$ and $\Gamma - K$ lines are oriented clockwise around the $K' - K - \Gamma - K'$ triangular contour. This generates (by continuity) a vortex centered on the diagonal, $\Gamma - M$, of the triangle. For the bilayer’s second-highest valence band, instead, the spins of the patches, along $K' - \Gamma$ and along $\Gamma - K$, are in the reversed directions, and their resultant has the same orientation as the pre-existing spins along the $K - K'$ BZ edge (Fig. A3). This produces an extended region of parallel spins (around M , and similarly around M') and no vortex. Hence, the presence of the vortex features, in Fig. 2, (and their absence in the spin texture of the second valence state in Fig. A3) is a consequence of the appearance of the patch features and their specific spin orientations.

Interestingly, compared to the spin textures of non-magnetic crystals, where the rules are that for \mathbf{k} parallel to a mirror plane M_i of the space group, one has $\mathbf{S}(\mathbf{k}) \perp M_i$, and for \mathbf{k} parallel to a rotation axis R_i , one has $\mathbf{S}(\mathbf{k}) \parallel R_i$, [14] here we have just the reversed behavior. In Fig. 2, we see that for \mathbf{k} parallel to the R_y axis, we have $\mathbf{S}(\mathbf{k}) \perp R_y$, and for \mathbf{k} parallel to the M_{xz} plane, we have $\mathbf{S}(\mathbf{k}) \parallel M_{xz}$. As will be shown in Section VII, this corresponds to two general rules for operators of a centrosymmetric system’s magnetic group that are combination of time reversal with a rotation operation, $R_i \cdot T$, or with a mirror-reflection operation, $M_i \cdot T$, namely: i)

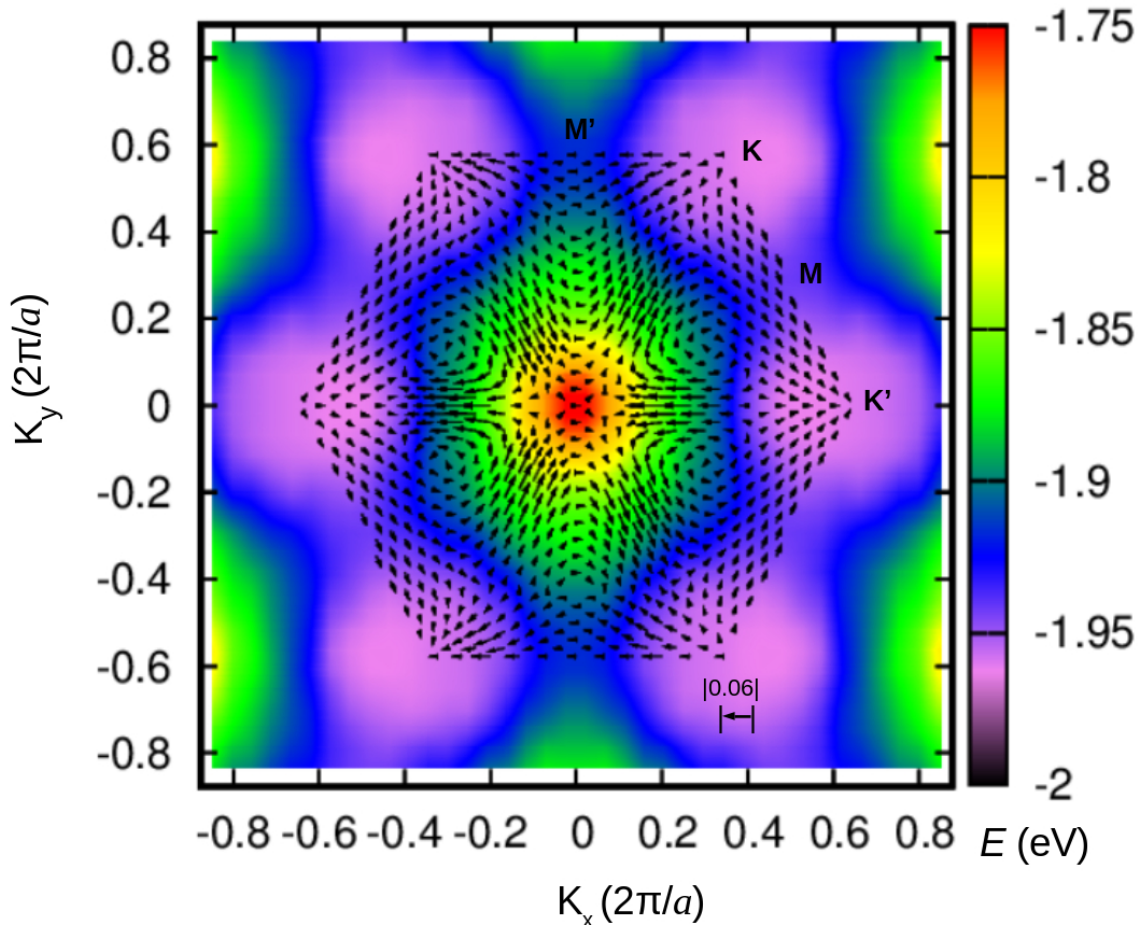


FIG. 2. In-plane spin texture plot in the 2D BZ for the highest valence band of the pristine FM CrI₃ bilayer. The magnitude of the in-plane spin component, $\mathbf{S}_{\parallel}(\mathbf{k})$, is proportional to the length of the arrow, according to the scale indicated in the bottom-right corner of the plot. The color map indicates the energies of the upper valence band in k -space.

for $\mathbf{k} \parallel R_i$, one has $\mathbf{S}(\mathbf{k}) \perp R_i$, ii) for $\mathbf{k} \parallel M_i$, one has $\mathbf{S}(\mathbf{k}) \parallel M_i$. In centrosymmetric systems, the rules are in fact reversed for rotation and reflection operations combined with time reversal, relative to the rules established for operators not involving time reversal.

VI. PLANAR-AVERAGED SPIN-POLARIZATION DENSITIES IN PRISTINE FM BILAYER

In Figs. 4 and 5, we display the planar averages of the probability density, $|\psi|^2(z)$, and spin-polarization density components, $m_x(z)$, $m_y(z)$, $m_z(z)$, for the highest and second-highest valence state at two different \mathbf{k} points chosen at similar distances from the BZ center, one on the k_x axis [Fig. 4] and the other one on the k_y axis [Fig. 5]. On the k_x axis, we took the point at $k_x = 0.2 \cdot 2\pi/a$, which is located within a $\mathbf{S}_{\parallel}(\mathbf{k})$ -patch region (see Fig. 2). On the k_y axis, we chose the point at $k_y = 0.3 \cdot 2\pi/a$, positioned in between two $\mathbf{S}_{\parallel}(\mathbf{k})$ -patch regions (see Fig. 2), out of which one with radial outward spin at $\mathbf{k}_+ = (0.2, 0.3) \cdot 2\pi/a$ and one with radial inward

spin at $\mathbf{k}_- = (-0.2, 0.3) \cdot 2\pi/a$. The chosen point on the k_y axis is observed to have the resultant (small) spin \mathbf{S}_{\parallel} oriented in the x -direction.

For \mathbf{k} along the k_x axis, in Fig. 4, the profiles of the probability density, $|\psi|^2(z)$, and of the spin-polarization-density components $m_x(z)$ and $m_z(z)$ are symmetric within the bilayer, i.e., with respect to the z -inversion at the midpoint between the two layers, l_1 , l_2 , of the bilayer. The $m_x(z)$ radial components (along \mathbf{k}) of the two states are seen to have similar amplitude and opposite signs, consistent with the sign reversal found for the patch spins $\mathbf{S}_{\parallel}(\mathbf{k})$ of the two bands. In addition, in Fig. 4, we observe for both states the presence of in-plane tangential $m_y(z)$ components of identical magnitude and opposite sign on l_1 and l_2 , which do not contribute to the $\mathbf{S}_{\parallel}(\mathbf{k})$ of the states. The magnitude of $m_y(z)$ is largest for the second state, and is comparable in that case to the magnitude of $m_x(x)$.

The in-plane tangential $m_{y(z)}$ components reverting sign from l_1 to l_2 , in Fig. 4, are consistent with a Rashba effect induced by the local vertical electric field, $\mathcal{E}_z^{(i)}$, on each layer l_i , due to the presence of the other layer. The

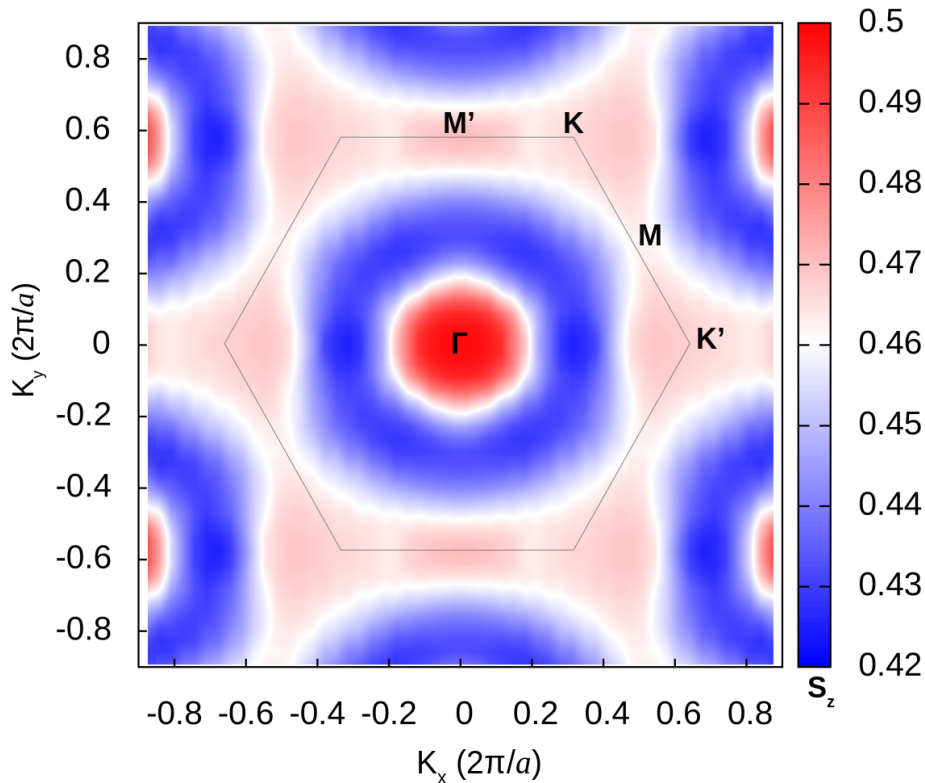


FIG. 3. Isovalue map of the out-of-plane spin component S_z in k -space for the upper valence band of the CrI₃ FM bilayer. The value of S_z is represented by the color scheme indicated on the right of the figure.

fields $\mathcal{E}_z^{(i)}$ are opposite on the two layers, and may be viewed in the phenomenological Rashba model as local magnetic effective fields $\mathbf{B}_{\text{eff}}^{(i)} \sim \mathbf{k} \times \mathcal{E}_z^{(i)}$ canting the spin polarization vectors in opposite directions on the two layers. In the AFM CrI₃ bilayer, similar in-plane tangential components of the spin polarization were found for the two highest (degenerate) valence states for \mathbf{k} around the BZ center.[43] In the latter case, however, the two states were segregated, each on one of the layer, and displayed opposite spin-polarization components. Here, instead, for the FM bilayer, the two opposite in-plane spin-polarization components on the two layers are found to co-exist in the same non-degenerate state.

For $\mathbf{k} = (0, 0.3) \cdot 2\pi/a$, in Fig.5, the planar averages reveal a striking asymmetry of the probability density $|\psi|^2(z)$ and of the out-of-plane spin-polarization component $m_z(z)$ on the two layers. They both exhibit a substantially larger weight on layer l_2 than on layer l_1 for the highest valence state, and the reversed trend for the second-highest valence state. Such an asymmetry is allowed by symmetry in our system at \mathbf{k} points with $k_y \neq 0$ (as will be seen in Section VII), but is unlike the behavior in nonmagnetic centrosymmetric crystals and in FM centrosymmetric systems without SOC. For $\mathbf{k} \parallel k_y$, in Fig.5, we also note that the $m_y(z)$ component is zero, and $m_x(z)$ is the only in-plane spin-polarization component present.

The $m_x(z)$ component in Fig. 5 is neither symmetric

nor antisymmetric, and appears to be the outcome of an interference for both states. This, in fact, can explain what is the mechanism controlling the weight difference in the probability density, i.e., an interference between the Rashba and non-Rashba effect. Indeed, we have seen that for $\mathbf{k} = (0, 0.3) \cdot 2\pi/a$, the S_{\parallel} for the upper valence band is along the k_x axis and has positive small S_x component (see Fig. 2), resulting from the continuation of spins between the two neighbouring non-Rashba spin patches $S_{\parallel}(\mathbf{k}_{\pm})$. The corresponding non-Rashba spin-polarization-density component, denoted $m_x^{\text{NR}}(z)$, has therefore to be globally (over the whole bilayer) positive for the upper valence state. Similarly, for the second state, with opposite orientation of S_{\parallel} (see Fig. A3), the $m_x^{\text{NR}}(z)$ component must be globally negative. At the same time, for \mathbf{k} along the k_y axis the Rashba-induced spin-polarization-density component is also expected to be in the x -direction. However, the corresponding $m_x^{\text{R}}(z)$ should be opposite on the two layers, i.e, negative on l_1 and positive on l_2 for both states (considering the orientation of the local electric fields $\mathcal{E}^{(1)}$ and $\mathcal{E}^{(2)}$, inferred from the Rashba $m_y(z)$ components at the other \mathbf{k} point, in Fig. 4). Hence for the first state, the Rashba $m_x^{\text{R}}(z)$ and the non-Rashba $m_x^{\text{NR}}(z)$ components are in phase on layer l_2 (both globally positive) and in counter-phase on layer l_1 (cancelling contributions), whereas for the second state, they are in phase on l_1 (globally negative) and in counter-phase on l_2 (mostly cancelling contributions),

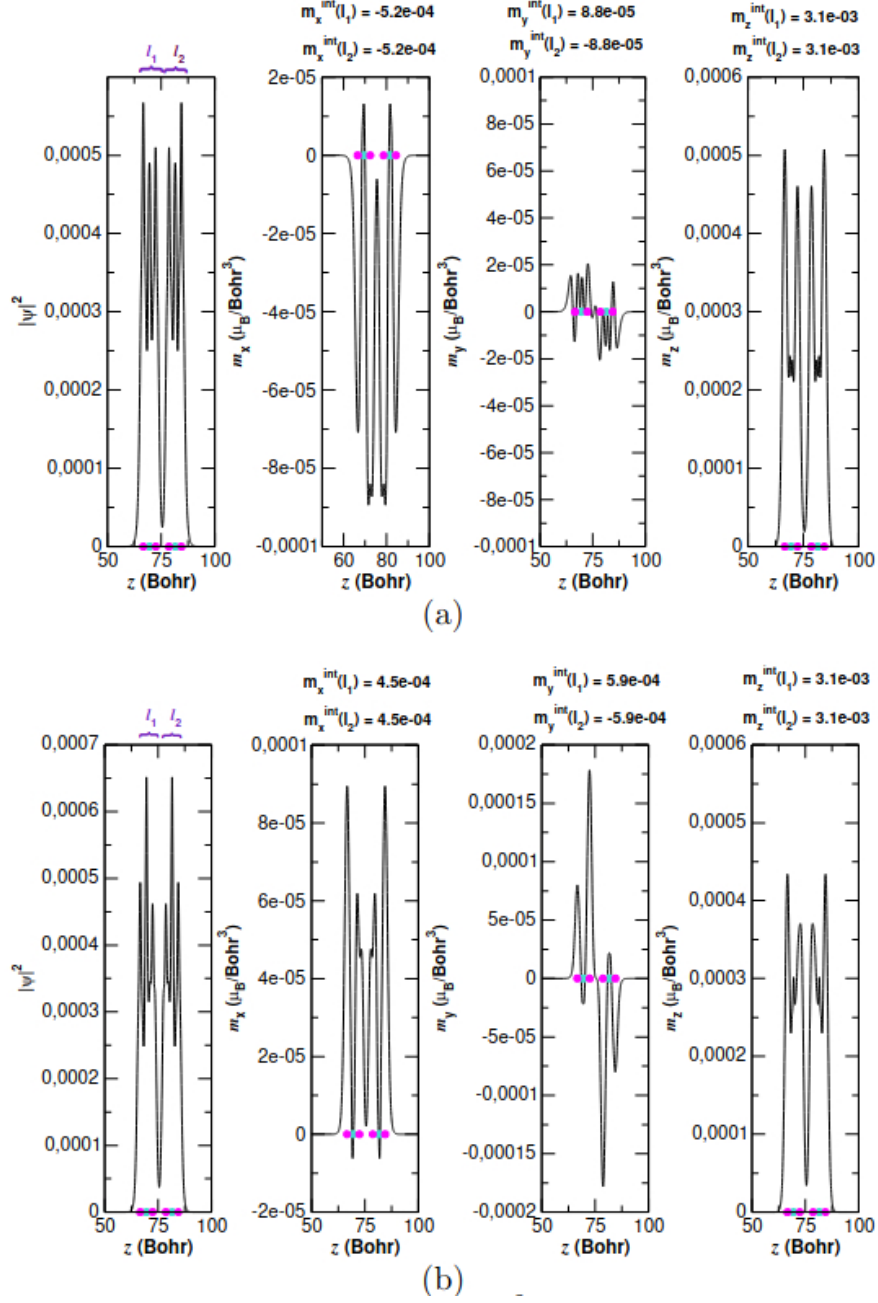


FIG. 4. Planar average of the probability density $|\Psi|^2$ and spin-polarization density components m_x , m_y and m_z calculated at $\mathbf{k} = (0.2, 0) \cdot 2\pi/a$ for the highest valence state (a) and second-highest valence state (b) of the FM bilayer. The turquoise and magenta circles show the positions of Cr and I atoms, respectively, along the z direction of the supercell; $m_\alpha^{\text{int}}(l_1)$ [$m_\alpha^{\text{int}}(l_2)$], $\alpha = x, y, z$, are obtained by integrating $m_\alpha(z)$ over half of the supercell length in the z -region starting [ending] at the mid-point between the two layers, l_1 and l_2 , and have units of μ_B/Bohr^2 .

consistent with the observed profiles of the final $m_x(z)$ components in Fig.5.

Furthermore, in the case of the first state, in Fig.5, the constructive interference of the Rashba effect and non-Rashba effect in $m_x(z)$ on layer l_2 and destructive one on layer l_1 are expected to favor (energetically) residence of that state on l_2 , shifting the probability-density weight to that layer. For the second state, instead, the constructive interference is on l_1 , shifting the weight to that layer.

This is in agreement with the trends in the weights of $|\psi|^2(z)$ and $m_z(z)$ observed, in Fig. 5, for both states.

VII. IMPLICATIONS OF FERROMAGNET SYMMETRIES ON SPIN TEXTURE

In order to better understand the pattern of the spin texture as well as the spatial behavior of the probability

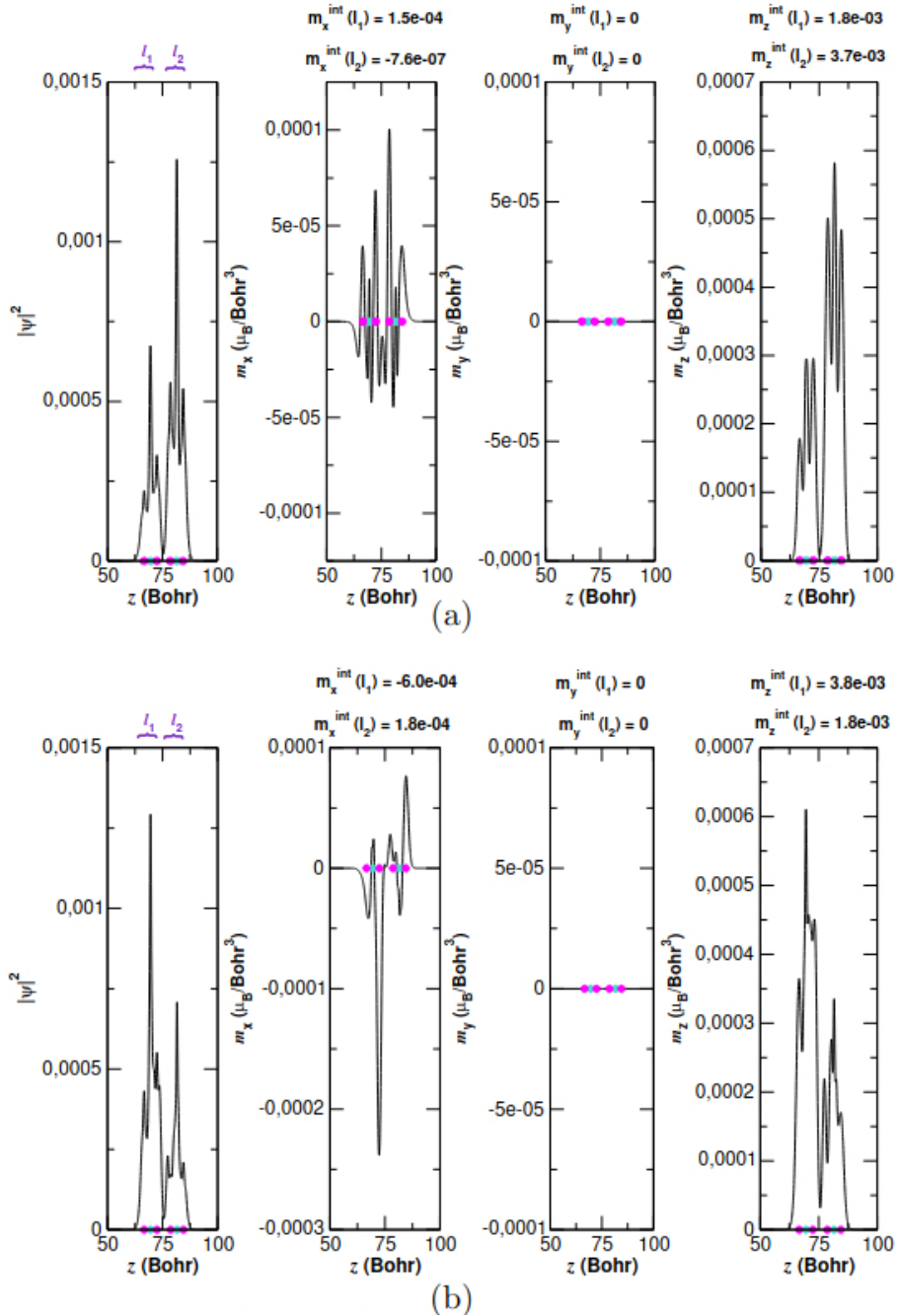


FIG. 5. Same as in Fig. 4, but calculated at $\mathbf{k} = (0, 0.3) \cdot 2\pi/a$.

density and spin-polarization densities in our prototype FM system, we have addressed their symmetry properties. We focus on non-degenerate states at \mathbf{k} points around Γ , i.e., with \mathbf{k} relative to the BZ center. To establish in general symmetry properties considering the operators of the magnetic group of a ferromagnet, we distinguish between operators involving time reversal and those which do not involve time reversal. The correspondence relations for the quantities \mathbf{S} , \mathbf{m} , and $|\psi|^2$ at \mathbf{k} points related by these different types of symmetry operators of a magnetic group are given in the Appendix.

In general, for an operator $\{R|\mathbf{f}\}$ that does not involve time reversal, i.e., where R is a spatial point-group operation and \mathbf{f} a fractional translation,[62] the symmetry correspondence relations are between \mathbf{k} and $R\mathbf{k}$, whereas for an operator $\{R'|\mathbf{f}'\}T$ combining a spatial operation $\{R'|\mathbf{f}'\}$ and time reversal, the symmetry relations are between \mathbf{k} and $-R'\mathbf{k}$ (see appendix A3). In particular, for the spin expectation values \mathbf{S} the relations are: I) $\mathbf{S}(R\mathbf{k}) = R\mathbf{S}(\mathbf{k})$ for an operator that does not involve time reversal, and II) $\mathbf{S}(-R'\mathbf{k}) = R'T\mathbf{S}(\mathbf{k})$ for an operator involving time reversal.

The spin expectation values \mathbf{S} and the spin-polarization density \mathbf{m} are axial vectors (vectors with a virtual current loop) and transform accordingly under time reversal and under spatial operations R, R' . [63] Taking this into account and using the operators of the magnetic group of the FM bilayer (see Section III) in the relations reported in the Appendix yields the correspondence rules, given in Table I, for the probability density, spin-polarization density, and spin expectation values in the FM bilayer at \mathbf{k} points related by the symmetry operators.

The symmetry operations E and I , in Table I, yield for the spin polarization vector, \mathbf{S} , as expected: $\mathbf{S}(-\mathbf{k}) = \mathbf{S}(\mathbf{k})$. Furthermore, considering the symmetry operators I and $M_{xz}T$, in Table I, the correspondence rule on \mathbf{S} implies that for \mathbf{k} points belonging to the M_{xz} plane ($k_y = 0$), the S_y component must be zero, and therefore $\mathbf{S}(\mathbf{k}) \parallel M_{xz}$. Similarly, considering the operators I and $R_y(180^\circ)T$, in Table I, the corresponding rule on \mathbf{S} imposes that for \mathbf{k} points on the R_y axis S_y must be zero, and thus $\mathbf{S}(\mathbf{k}) \perp R_y$. This is in agreement with the behavior noted in Section V, where the two rules were anticipated.

Conspicuously, for non-degenerate states with wavevector \mathbf{k} , the above relation (II) $\mathbf{S}(-R'\mathbf{k}) = R'T\mathbf{S}(\mathbf{k})$ is valid in general for any operator $\{R'|\mathbf{f}'\}T$ of a system's magnetic group. More generally therefore, with 3D \mathbf{k} vectors and any operators $\{M_i|\mathbf{f}'\}T$ and $\{R_i|\mathbf{f}''\}T$ of the magnetic group of a centrosymmetric system that are, respectively, reflection and rotation operations combined with time reversal, the relation (II) yields that for $\mathbf{k} \parallel M_i$, $\mathbf{S}(\mathbf{k}) \parallel M_i$, and for $\mathbf{k} \parallel R_i$, $\mathbf{S}(\mathbf{k}) \perp R_i$. This is the reverse of the rules established for non-magnetic systems, where for $\mathbf{k} \parallel M_i$, one has $\mathbf{S}(\mathbf{k}) \perp M_i$, and for $\mathbf{k} \parallel R_i$, $\mathbf{S}(\mathbf{k}) \parallel R_i$, as obtained with operators not involving T . In centrosymmetric systems thus in general, time reversal is reverting those rules.

Furthermore, a notable consequence of the relation (I) is that for any CrI_3 bilayer structure which is non chiral (but has the same vertical FM alignment of the Cr spins), the in-plane spin texture of the FM bilayer $\mathbf{S}_{\parallel}(\mathbf{k})$ must be zero at all \mathbf{k} points. Indeed, such non-chiral FM bilayers are characterized by a horizontal mirror symmetry operator $\{M_{xy}|\mathbf{f}\}$ in their magnetic group. The corresponding relation (I) yields $M_{xy}\mathbf{S}_{\parallel}(\mathbf{k}) = \mathbf{S}_{\parallel}(M_{xy}\mathbf{k}) = \mathbf{S}_{\parallel}(\mathbf{k})$ for \mathbf{k} in the 2D BZ, and considering that an axial vector $\mathbf{S}_{\parallel}(\mathbf{k})$ parallel to the mirror plane transforms as $M_{xy}\mathbf{S}_{\parallel}(\mathbf{k}) = -\mathbf{S}_{\parallel}(\mathbf{k})$, this implies that $\mathbf{S}_{\parallel}(\mathbf{k}) = 0$.

Concerning the probability density, $|\Psi_{\mathbf{k}}|^2$, the symmetry relation obtained with E and $R_y(180^\circ)T$, in Table I, imposes that for \mathbf{k} along the k_x axis, the planar average, $|\psi|^2(z)$, must be symmetric under inversion through the z mid-point between the two layers. However, when $k_y \neq 0$, in Table I, the probability-density weight may differ on the two layers, as we noticed in Section V (see also the layer-projected band structure in SI). This is in contrast to the case of non-magnetic centro-symmetric crystals, where the probability density at any \mathbf{k} point $\rho_{\mathbf{k}}(\mathbf{r})$ [given by $\rho_{\mathbf{k}}(\vec{r}) = \sum_i |\psi_{i,\mathbf{k}}(\mathbf{r})|^2$, with the sum over the

set of degenerate states at \mathbf{k}] is symmetric under inversion $\rho_{\mathbf{k}}(\mathbf{r}) = \rho_{\mathbf{k}}(-\mathbf{r})$, due to the additional time-reversal invariance of the system.

VIII. MECHANISMS OF INTERLAYER-INDUCED SPIN TEXTURE

The symmetry rules of the previous section have explained some properties of the spin texture of the FM bilayer and have shown that the in-plane spin texture is related to the chirality of the two layers (as a whole, as well as the intrinsic chirality of each monolayer). These rules do not explain however the intensity behavior of the in-plane spin texture and the mechanism generating the spin-patch features with opposite spins for the two highest valence bands. In this section, we discuss the mechanisms of in-plane canting of the spin-polarization density $\mathbf{m}_{\mathbf{k}}$ on the two CrI_3 layers, caused by the interlayer interaction, and address the origin of the opposite patch spins for the two highest valence bands.

We have seen, in Sections V and VI, that two effects of the interlayer interaction are present, around the BZ center, which cant the spin polarization $\mathbf{m}_{\mathbf{k}}^{l_i}$ away from the z axis on the layers l_1 and l_2 : the Rashba-related effect and the non-Rashba (chiral) effect, the latter leading to the spin patches. For \mathbf{k} along the k_x axis, the Rashba effect induces opposite spin-polarization components $m_y^{l_1}$, $m_y^{l_2}$ on the two layers, for both states; whereas the other effect induces identical components $m_x^{l_1}$, $m_x^{l_2}$ on the two layers, but having opposite sign for the two states. In the following, considering different components of the interaction between the layers, and based on the nature of the monolayer main states involved and their perturbation, we rationalize the behavior of the spin texture around Γ , singling out the coupling between states that can account for the spin-patch behavior and for the Rashba behavior of the two upper valence states on the two layers.

To do that we have first determined the main changes induced by the interlayer interaction in the highest valence states of the bilayer for \mathbf{k} along the $\Gamma - K'$ and $\Gamma - K$ directions (relevant for the spin patches). The relativistic band structure of the FM bilayer is plotted in Fig. 6 and that of the FM monolayer in the Appendix (Fig. A2). The two highest valence bands of the bilayer have dispersions resembling that of the monolayer. These bands can be viewed as a superposition of the highest-valence band of the two isolated monolayers, with some additional k -dependent splitting and smooth rise in band energy away from the BZ center, caused by the interlayer interaction. For the monolayer, the valence-band edge in the central part of the BZ corresponds to I-5p spin-orbital $|J = 3/2, J_z = +3/2\rangle$ states, with some small additional I-5p $|J = 3/2, J_z = -1/2\rangle$ component incorporated when moving away somewhat from Γ , i.e., for k radii $0.2 - 0.3 \cdot 2\pi/a$. The resulting states of the monolayer have vanishing in-plane spin $\mathbf{S}_{\parallel}(\mathbf{k})$, given the rule for non-zero matrix elements of the $\hat{\sigma}_x$ and $\hat{\sigma}_y$ operators: $\langle J, J_z | \hat{\sigma}_\alpha | J, J'_z \rangle \neq 0$ for $\alpha = x, y$, only when

$$\Delta J_z = J_z - J'_z = \pm 1.$$

In the bilayer band-structure plots, in Fig. 6, we display along the bands the I-5p spin-orbital characters projecting on the I-5p $J = 3/2$ atomic states with $J_z = +3/2, +1/2, -1/2,$ and $-3/2$ in panels (a), (b), (c), and (d), respectively — the same is reported for the monolayer in the Appendix. Note that the I-5p $J = 1/2$ states are located at lower energy than the I-5p $J = 3/2$ states seen in Fig. 6, due to the large I-5p atomic spin-orbit splitting (0.9 eV).[51] Near the BZ center, the two upper valence bands of the bilayer have nearly complete I-5p, $J = 3/2, J_z = +3/2$ character, as in the monolayer, see Fig. 6(a). These bands correspond to the highest I-5p $|J = 3/2, J_z = +3/2\rangle$ states of the monolayers, Fig. A2(a), and split at (and near) the Γ point into antibonding and bonding states (respectively odd and even under inversion at Γ) due to the interlayer potential ΔV . Comparison of the projected characters in the bilayer and monolayer along the $\Gamma - K$ and $\Gamma - K'$ directions indicates as main change, due to the interlayer interaction, the inclusion of an I-5p $|J = 3/2, J_z = +1/2\rangle$ component in the two highest valence states of the bilayer, for $k \approx 0.2 - 0.3 \cdot 2\pi/a$, corresponding to the spin patches. At the same time the weight of the I-5p component $|J = 3/2, J_z = -1/2\rangle$ of these two states also somewhat increases with respect to that of the monolayer at those k radii.

It is important to note that inclusion of the $|J = 3/2, J_z = +1/2\rangle$ component in the highest-valence states of the bilayer, in Fig. 6(b), is essential for the occurrence of the in-plane spin components $m_{\parallel}^{l_i}$ on the two layers, as it gives rise to non-vanishing matrix elements $\langle J, J_z | \hat{\sigma}_\alpha | J, J'_z \rangle$ for $\alpha = x, y$. This applies to both the Rashba-related and the spin-patch canting effects in the central part of the BZ.

Starting thus from the relevant $|J = 3/2, J_z = 3/2\rangle$ and $|J = 3/2, J_z = 1/2\rangle$ basis states of the two isolated monolayers at fixed \mathbf{k} along the $\Gamma - K'$ direction, and considering as perturbations the local electric field $\mathcal{E}^{(i)}$ and the chiral component of the interlayer potential, in the Appendix we determine which intra and interlayer coupling components among the basis states are compatible with the canting behavior found on the two layers for the upper two valence states of the bilayer. The type of coupling terms involved in the Rashba and chiral interlayer-potential effect are schematically displayed in Fig. 7. In the following we discuss separately these two types of coupling and canting, and their consequences on the electronic states.

VIII.1. Spin-canting induced by Rashba term

To describe in general the effect of an electric field \mathcal{E}_z on the $J = 3/2$ states of the monolayer, the most appropriate model description, in view of the large I-5p SOC, is provided by the orbital Rashba Hamiltonian $H_R^L = -\mathbf{d}_L \cdot \mathcal{E}_z = -\gamma(\mathbf{k} \times \mathcal{E}_z) \cdot \mathbf{L}$, where $\mathbf{d}_L = \gamma(\mathbf{L} \times \mathbf{k})$ is the electronic dipole moment created by the asym-

metric charge distribution,[64] and γ is a proportional constant. Here we are specifically interested in the perturbation effect of the local electric field \mathcal{E}_z on the $|J = 3/2, J_z = +3/2\rangle$ states of the monolayer upper-valence band. In that case, we note that the coupling and the perturbation effect on the upper valence states are actually the same (within a proportionality constant) to those obtained using the phenomenological Rashba spin Hamiltonian $H_R^k = -\mathbf{d}_L \cdot \mathcal{E}_z = -\lambda(\mathbf{k} \times \mathcal{E}_z) \cdot \boldsymbol{\sigma}$, with λ taken as a constant for those states. In the following, when using 'Rashba term' we refer in principle to H_R^L , but the same is obtained with H_R . The local electric field \mathcal{E}_z on one monolayer is a measure of the local asymmetry (for that monolayer) in the electrostatic potential induced by the other CrI₃ monolayer.

Figure 7(a) shows a schematic representation of the Rashba interaction and its effect in a Löwdin perturbation approach on the highest valence state of each layer (denoted by $|A\rangle$ and $|A'\rangle$ in layer 1 and 2, respectively). The local electric fields on the two layers are opposite, as mentioned earlier. For \mathbf{k} around Γ , the Rashba (on-site) term couples the upper I-5p $|J = 3/2, J_z = +3/2\rangle$ state of each layer with the $|J = 3/2, J_z = +1/2\rangle$ state of the same layer (non-zero coupling is obtained only for $\Delta J_z = \pm 1$). The interacting bands are denoted in Fig. A2. The $|A\rangle$ state interacts thus, via the Rashba term, with the $|B\rangle$ state from layer 1, and the $|A'\rangle$ state with the $|B'\rangle$ from layer 2. This coupling induces opposite components $i\alpha |B\rangle$ and $-i\alpha |B'\rangle$ in the upper states ($|A\rangle$ and $|A'\rangle$) of the two layers, because of the opposite local electric fields on the two layers (with α real, see Appendix A4). It also shifts to higher energy the upper energy level of each layer (with a shift proportional to $|k|^2$).

The upper two states with equal energy of the two layers combine then in bonding and antibonding states, as indicated schematically in Fig. 7(a). The two resulting bonding- and antibonding states display in-plane spin components which are opposite on the two layers (see Appendix A2). This is consistent with the behavior found in Section V, i.e., coexistence of opposite spin-polarization components on the two layers in the same non-degenerate state.

For convenience, in the scheme shown in Fig. 7(a), we introduced the Rashba coupling first and then the coupling induced by the interlayer potential between the $|A\rangle$ and $|A'\rangle$, which gives rise to the bonding and antibonding split states. However, this order is not really relevant in the Löwdin perturbation approach. The same types of final upper two states and conclusions are obtained with the reversed order in the perturbations, i.e., starting from the coupling giving the bonding-antibonding split states for the A-type and for the B-type bilayer states and then introducing the H_R or H_L coupling.

Regarding the bonding and antibonding states, we note that the presence of Rashba components in the orbitals $|A\rangle + i\alpha |B\rangle$ and $|A'\rangle - i\alpha |B'\rangle$ on the two layers does not affect the energy of the resulting bonding and antibonding states to first order in α . However, when k

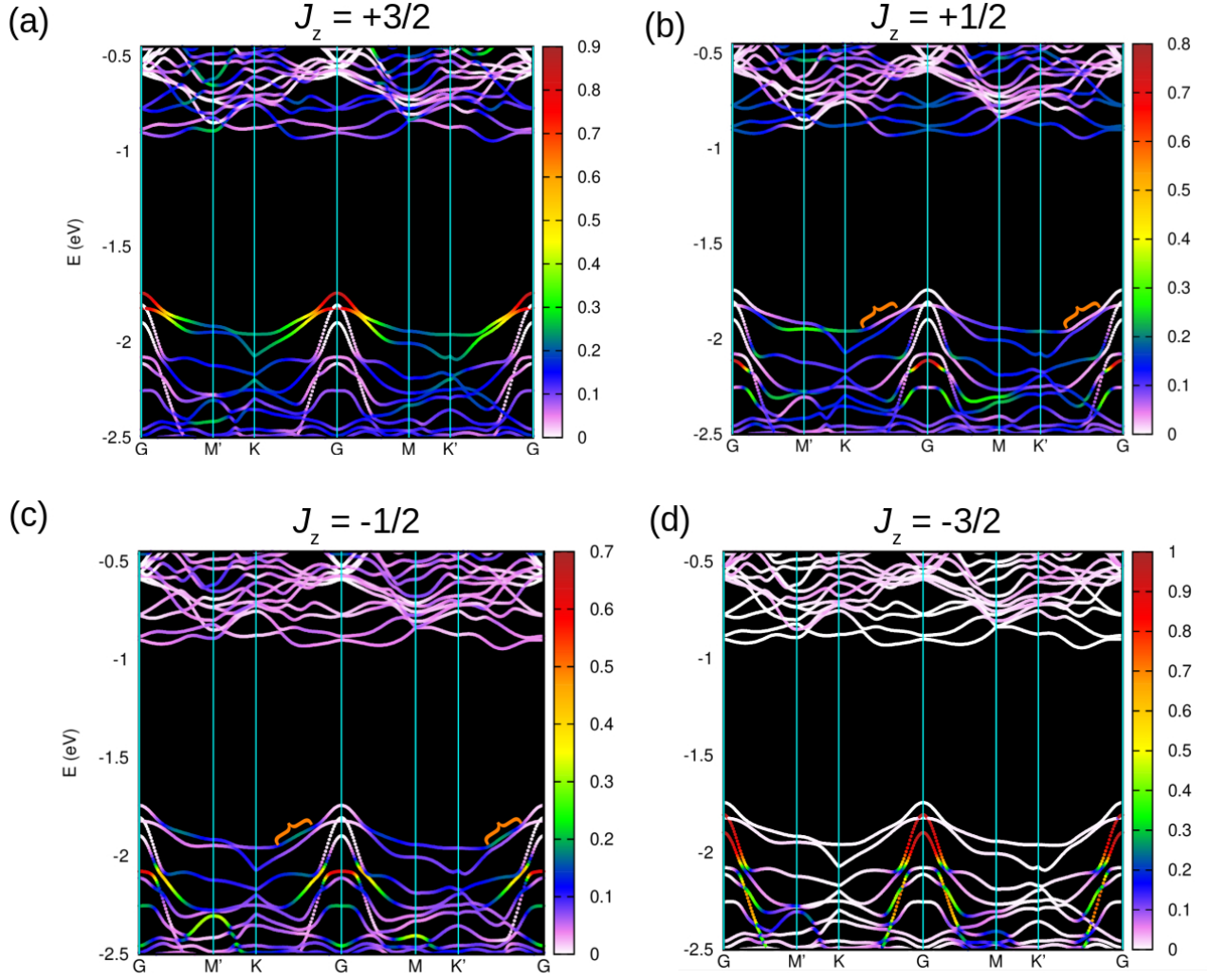


FIG. 6. Relativistic band-structure plots for the CrI₃ FM bilayer with projected I-5*p* atomic spin-orbital characters. The projections are on I-5*p* $J = 3/2$ atomic states with $J_z = +3/2$ (a), $J_z = +1/2$ (b), $J_z = -1/2$ (c), and $J_z = -3/2$ (d). The energy window includes the highest valence bands and lowest conduction bands. The band-structure regions corresponding to the spin patches along $\Gamma - K$ and $\Gamma - K'$ are shown by the orange symbols in (b) and (c).

increases and the Rashba components become significant, the magnitude of the $|A\rangle$ and $|A'\rangle$ components will tend to decrease due to normalisation. This in turn will increase the energy of the bonding state and decrease that of the antibonding state (to second order in α). This provides a qualitative explanation for the decrease in the splitting between the antibonding and bonding state with increasing k one observes around Γ in Fig. 6.

We would like also to emphasize that, although one may use for simplicity the phenomenological Rashba Hamiltonian H_R for the coupling, in order to understand within a DFT framework what may be the microscopic origin of the canting, it is appropriate to go back to the orbital Rashba description: $H_L = -\mathbf{d}_L \cdot \mathbf{E}_z$ with $\mathbf{d}_L = \gamma(\mathbf{L} \times \mathbf{k})$. The orbital Rashba description highlights as driving force for the canting the alignment of the electric dipole moments with the electric field \mathbf{E}_z , [64] which in turn requires a mixing/coupling between $|J = 3/2, J_z\rangle$

spin-orbital eigenstates (with $\Delta J_z = \pm 1$).

VIII.2. Spin canting induced by interlayer chiral potential

The chirality of the layer stacking in the bilayer leads to an interlayer potential ΔV which includes also a chiral component (as defined in Section III). As pointed out in that section, there are three special directions associated with the structural chirality of the bilayer, which correspond to the directions in which the body diagonals of the Iodine octahedra of the two layers are aligned (see Fig. 1). These three directions are tilted relative to the z axis with the same tilt angle, and their projections on the xy plane [schematically drawn in Fig. 1(b)] are along the $\Gamma - K'$ and $\Gamma - K$ directions of the BZ.

Figure 7(b) shows a schematic view, for \mathbf{k} along the $\Gamma - K'$ direction, of the coupling induced by the chi-

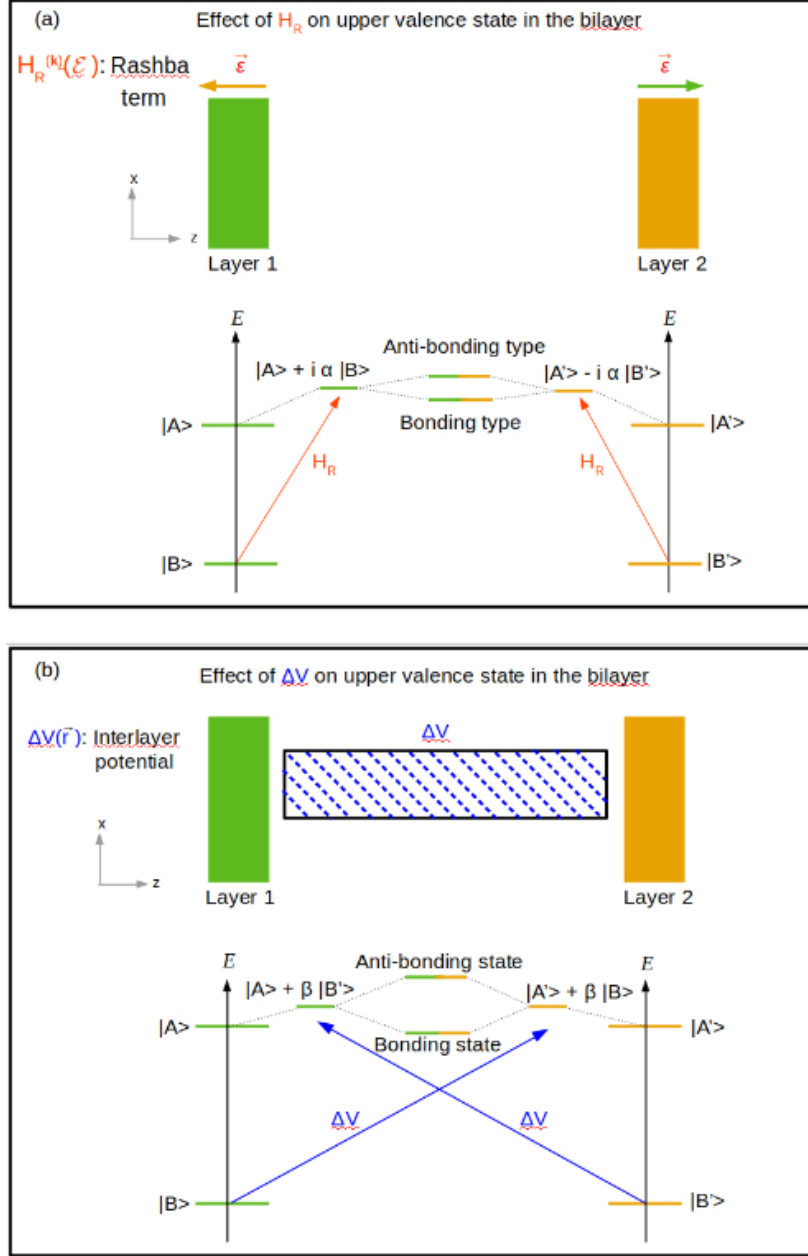


FIG. 7. Schematics of interlayer Rashba (a) and chiral potential (b) interactions in the FM bilayer and their perturbative effects on the highest valence states of the monolayers, at fixed \mathbf{k} along the k_x axis (near Γ). $|A\rangle$ and $|B\rangle$ ($|A'\rangle$ and $|B'\rangle$) stand for the eigenstates of the monolayer 1 (2). Rashba interaction arises due to the electric field \mathcal{E} generated on layer 1 due to layer 2. The Rashba term, H_R , produces a coupling between eigenstates of the same monolayer. This coupling induces opposite components in the states of the two layers, and shifts their energy level. The chiral interlayer potential ΔV couples eigenstates from different monolayers. This term induces identical components in the states of the two layers, and shifts their energy level. The bonding and antibonding states resulting from (b) [(a)] account for the properties of the m_x [m_y] spin-polarization components observed on the two layers for the two upper valence states of the bilayer.

ral potential ΔV and its effect on the highest valence states of the two layers, in a Löwdin-type perturbation approach. ΔV couples the $|J = 3/2, J_z = +3/2\rangle$ state of layer 1 (hereafter the $|A\rangle$ state) with the $|J = 3/2, J_z = +1/2\rangle$ state of layer 2 (the $|B'\rangle$ state). Similarly, the $|J = 3/2, J_z = +3/2\rangle$ state of layer 2 (the $|A'\rangle$ state) couples with the $|J = 3/2, J_z = +1/2\rangle$ state of layer 1

(the $|B\rangle$ state). In fact, ΔV couples the same types of states as the Rashba term, with the distinction that here the interacting states reside on different layers. The interaction occurs between the p_x orbital of one monolayer and the p_z orbital of the other monolayer having the same spin (see Appendix A4.1). Since the interlayer potential is real, the coefficient of the coupled $|B'\rangle$ component is

real—in contrast to the coefficient of $|B\rangle$ for the Rashba effect, which is purely imaginary at the same \mathbf{k} . The chiral coupling shifts to higher energy the level of the two upper degenerate states.

The two degenerate states then combine, as also indicated in Fig. 7(b), to give an antibonding and a bonding state (due to the coupling induced by ΔV between $|A\rangle$ and $|A'\rangle$). The resulting bonding state displays radial spin-polarization components which are identical on the two layers, $m_x^{l_1} = m_x^{l_2}$, while the antibonding state exhibits the reversed spin-polarization components on the two layers, $-m_x^{l_1}, -m_x^{l_2}$ (see Appendix). This rationalization, based on the off-site couplings $\langle A|\Delta V|B'\rangle = \langle A'|\Delta V|B\rangle$ caused by the chiral potential, accounts for the spin-polarization behavior observed, in Section V, for the two upper valence states in the spin patch regions along the $\Gamma - K'$ direction.

Analogous arguments hold for the spin patches along the other special directions rotated by $\pm 120^\circ$ from the k_x axis. It should be noted that an onsite coupling with ΔV between the $|J = 3/2, J_z = +3/2\rangle$ and $|J = 3/2, J_z = +1/2\rangle$ states (as is the case of the Rashba-canting effect) would not account for the observed m_x spin-polarization behavior, as the spin-polarization would be the same for the two upper valence states.

Similar to the Rashba-canting discussion, for simplicity the order of the perturbations has been taken with first the non-zero A - B coupling and then proceeding with the coupling for the bonding and antibonding states. As in the Rashba case, however, the final upper two states and conclusions are the same using the reversed order in the perturbations. It is important to note that the two effects (Rashba and chiral) co-exist in the upper valence states, because these effects derive from matrix elements between different basis states of the unperturbed system, e.g., $\langle A|H_L|B\rangle$ versus $\langle A|\Delta V|B'\rangle$ corresponding to different off-diagonal elements in the Löwdin matrix-perturbation approach. The final two upper valence states are the bonding and antibonding combinations of $|A\rangle + \beta|B'\rangle + i\alpha|B\rangle$ and $|A'\rangle + \beta|B\rangle - i\alpha|B'\rangle$.

Finally, we would like to emphasize that it is only in the main central part of the BZ (including the patch regions) that the behavior of the spin texture is dominated by the contributions of the iodine $5p$ states discussed in this section. For larger k radii, i.e., beyond the patch regions, the weight of the iodine states strongly decreases, while the weight of the Cr $3d$ states becomes substantial.[51] Hence, both the Rashba and chiral interlayer-potential effects are expected to vanish at large k radii, as one observes in Fig. 2 (and indirectly in Fig. 3).

IX. MANIPULATION OF SPIN TEXTURE WITH VERTICAL COMPRESSIVE STRAIN

We have seen that the highest valence band of the FM bilayer is characterized by a rich in-plane spin texture, with vortices and spin patches induced by the interlayer interaction. We also saw that, although the Rashba ef-

fect does not directly contribute to the (space-integrated) in-plane spin texture, it penalizes in energy the bonding states relative to the antibonding states around Γ . All these effects are expected to be intensified when applying a vertical compression on the bilayer, possibly even leading to a valence band-edge states with canted spin. In fact, we found previously that new valence band maxima appear outside Γ , along the $\Gamma - M'$ lines of the BZ, when the FM bilayer is vertically compressed.[51] Here we address the corresponding spin texture.

Figure 8 shows the in-plane spin texture for the upper valence band of the FM bilayer with 5% compressive strain applied along the vertical direction. The iso-energy map of the band is also displayed in this figure. The compressive strain clearly modifies considerably the in-plane spin-texture pattern and enhances the spin canting, in particular along the $\Gamma - K'$ directions. One can observe that the spin patches have been elongated and made much thinner by compression, which also brought the vortices much closer to the BZ center. This gives rise to a “flower-like” pattern in the spin texture around Γ in Fig. 8. Strong S_x components are also present at and in the vicinity of the high symmetry M' point. The two valence band maxima located along the $\Gamma - M'$ directions, in Fig. 8, display significant S_x -spin components. Local valence band maxima outside Γ are also present along the $\Gamma - M$ directions and show non-negligible in-plane spins. Hence, the vertical compression produces valence band-edge states with notable in-plane spin canting in the bilayer.

The largest value of $|\mathbf{S}_{\parallel}(\mathbf{k})|$ appears at $k_x = 0.33 \cdot 2\pi/a, k_y = 0$, in Fig. 8, and is 0.107. At that \mathbf{k} point, the amplitude of the in-plane component is 25% of that of the $S_z(\mathbf{k})$ component (shown in the SI). Therefore, the largest ratio of in-plane to out-of-plane spin components is substantially increased upon application of the compressive strain. We note that, as in the case of the pristine bilayer, the second highest-valence band displays strong in-plane components along or in the vicinity of the $\Gamma - K'$ and $\Gamma - K$ lines (see SI), with reversed sign relative to the highest valence state. The in-plane spins of the second state are also oriented in the opposite direction, compared to the first state, in the regions of the local valence band maxima of Fig. 8.

One can notice, in Fig. 8, that the in-plane spin is larger along the special $\Gamma - K'$ and $\Gamma - K$ lines than in any other region in the central part of the BZ. As in the case of the unstrained system, we view the vortex features as a consequence of the strong radial spins produced by the chiral potential along these special directions. The concentration of vortex features closer to Γ is attributed mainly to the intensification of the in-plane chiral spins along those directions at $k \sim 0.2 \cdot 2\pi/a$ (relative to the BZ-edge spins), which shifts the centers of the vortices towards the BZ center. This shift, however, is also correlated with a peculiar change of the upper valence band in the central part of the BZ (see below).

Figure 9 shows the projected band-structure plots for the bilayer with 5% compression projecting on the iodine

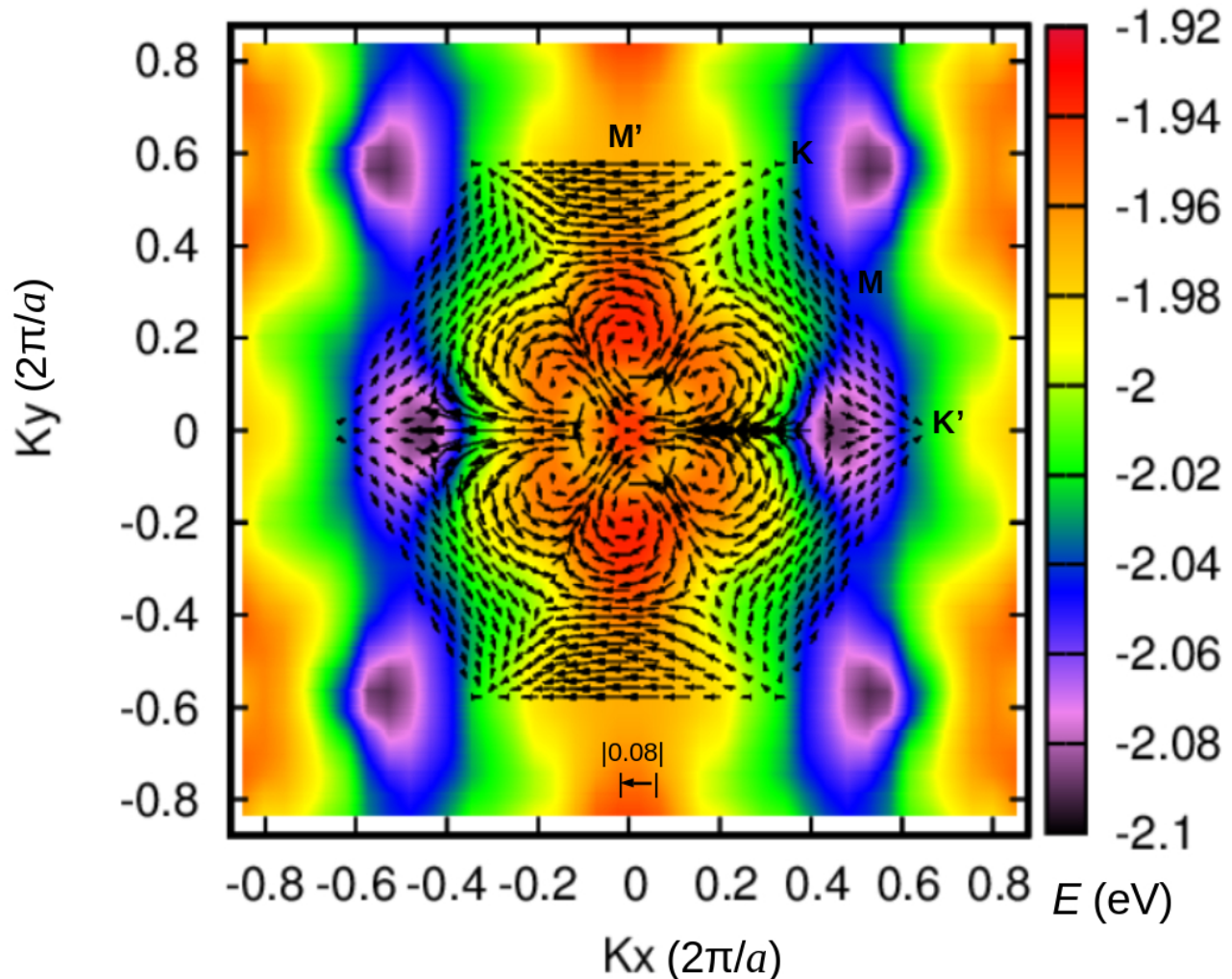


FIG. 8. Same as in Fig. 2, but for the FM bilayer with 5% vertical compression.

$J = 3/2$ atomic states with $J_z = +3/2$ (a), $J_z = +1/2$ (b), $J_z = -1/2$ (c), and $J_z = -3/2$ (d). Consistent with the Rashba and chiral coupling discussed in Section VIII, one observes that the valence-band maxima appearing along $\Gamma - M'$, with canted spin in Fig. 8, display strongly mixed $J_z = +3/2$ and $J_z = +1/2$ characters [see Figs. 9(a) and (b)]; in fact under compression the $J_z = +1/2$ component became the dominant one at the VBM. Similarly, the highest valence states outside Γ , along the $\Gamma - M$, $\Gamma - K$, and $\Gamma - K'$ direction, with canted spins in Fig. 8, all have strongly mixed $J_z = +3/2$ and $J_z = +1/2$ character.

One observes, in Fig. 9, that under compression the band that corresponds to the VBM outside Γ sinks in energy when approaching Γ , unlike the band that has the highest valence energy at the BZ center. The band which lowers its energy, and has second-highest $J_z = +3/2$ character at and near Γ , corresponds to interlayer bonding states, whereas the other band, with largest $J_z = +3/2$ weight at Γ , corresponds to the antibond-

ing counterparts. Compression increases the bonding-antibonding splitting at Γ , as expected for layers coming closer to each other. Interestingly, however, the bonding-band states experience outside Γ a rapid increase in energy with increasing k radii, which we attribute largely to the Rashba effect, which penalizes the bonding state relative to the antibonding one.

X. CONCLUSIONS

In this work we have studied the spin-polarization canting effects and momentum spin-texture properties in a 2D centrosymmetric ferromagnet with perpendicular magnetization, based on DFT calculations. Using as an example the spin textures of the highest valence bands of the CrI_3 FM bilayer, we have shown the existence of two distinct relativistic spin-polarization canting effects related to the interlayer interaction.

The first effect derives from the 'chiral' character (lack

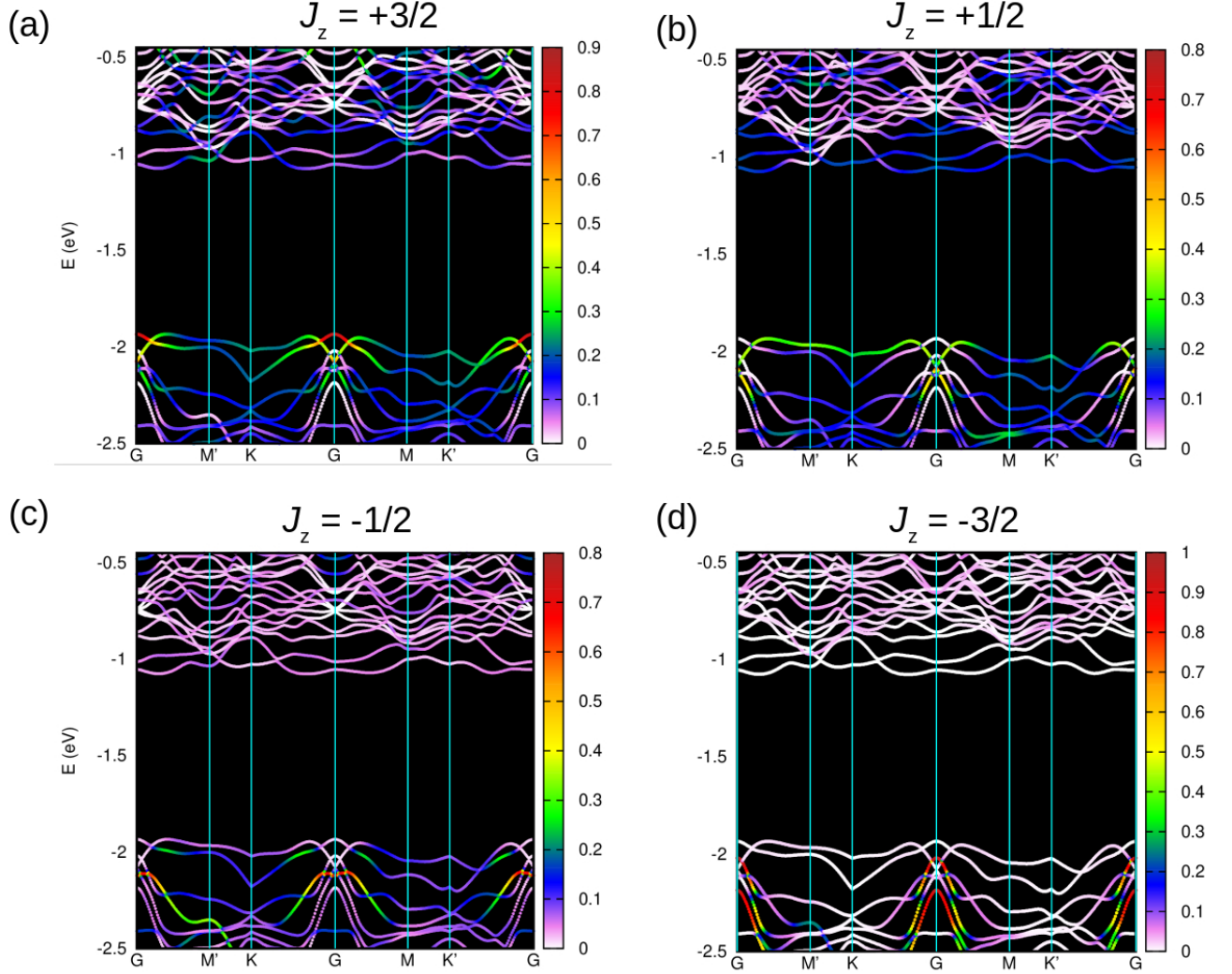


FIG. 9. Same as in Fig. 6, but for the CrI_3 FM bilayer with 5% compressive strain.

of reflection symmetry between the two layers) of the interlayer potential, combined with the spin-orbital polarized nature of the highest valence states. This effect is found to induce on both layers of the bilayer the same in-plane spin-polarization canting. In the case of the upper valence band of the CrI_3 FM bilayer, this produces radial “spin-patch” features in the in-plane-spin texture along specific chiral directions of the BZ. The second effect is a Rashba-related spin-polarization canting, caused by the electric field on each layer due to the presence of the other layer. Interestingly, in the case of a centrosymmetric ferromagnet this effect induces within the same electronic state opposite spin-polarization canting on the two layers. This results in an energy-penalization effect for bonding states relative to antibonding states in a centrosymmetric ferromagnet.

Furthermore, using the FM bilayer as an example, we have provided some general rules for centrosymmetric systems imposed on the momentum spin texture by magnetic-group symmetry operators. We have shown that symmetry operators that combine time reversal with

rotations and reflections in magnetic-space groups of centrosymmetric systems give rise to rules for the spin polarization vector in the BZ which are reversed with respect to those established for non-magnetic groups; namely they impose that spin-polarization vectors must be parallel to mirror planes and perpendicular to rotation axes for such operators.

In addition, exploiting the above FM chiral and Rashba effects, we have shown for the CrI_3 FM bilayer that perpendicular compressive strain can be used to effectively manipulate the spin texture. In particular, our *ab initio* calculations for the CrI_3 FM bilayer show that vertical compression induces valence-band-edge states with canted spin polarization.

The chiral and Rashba spin-canting FM effects disclosed in the present study are expected to be observed also in other 2D centrosymmetric FM bilayers with SOC and, respectively, chiral layer stacking and semiconductor character. Furthermore, the present rules on spin textures for centrosymmetry systems imposed by magnetic-group operators complement those established for the

non-magnetic materials, and are expected to be helpful guidelines for the shapes of spin textures in BZ's of such magnetic materials in general.

A. APPENDIX

A1. CrI₃ FM monolayer: spin texture and projected band structure

Figure A1 shows the in-plane spin texture for the highest valence band of the CrI₃ FM monolayer. The in-plane spin texture is seen to be non-negligible essentially only near the BZ edges. The highest magnitude of the in-plane spin, \mathbf{S}_{\parallel} appear in close vicinity of the M and M' points and is 0.021.

The spin-texture pattern observed along the contour of the BZ, in Fig. A1, with spins parallel to the BZ edges, is imposed by the symmetry rules of Section VII, for the magnetic group $D_{3d}[S_6]$ of the monolayer. This group includes, in particular, the symmetry operators $R_y(180^\circ) \cdot T$, where time reversal is combined with the two-fold rotations about the y and equivalent directions (along the $\Gamma - M$, and $M' - \Gamma$ directions). The corresponding symmetry rules impose that for $\mathbf{k} \parallel \Gamma - M^{(\prime)}$, $\mathbf{S}(\mathbf{k}) \perp \Gamma - M^{(\prime)}$. Furthermore, the monolayer group also includes the symmetry operators $R_z(\pm 60^\circ) \cdot M_{xy}$. The corresponding symmetry rules impose that $\mathbf{S}_{\parallel}(M') = -R_z(60^\circ)\mathbf{S}_{\parallel}(M)$.

We note that the monolayer magnetic group also contains the symmetry operators $M_d \cdot T$, where time reversal is combined with the reflections about vertical mirror planes parallel to the x axis and equivalent directions ($\Gamma - K'$ and $K - \Gamma$). The corresponding symmetry rules imply that for $\mathbf{k} \parallel \Gamma - K^{(\prime)}$, $\mathbf{S}_{\parallel}(\mathbf{k}) \parallel \Gamma - K^{(\prime)}$.

Figure A2 shows the projected band-structure plots for the CrI₃ FM monolayer projecting on the iodine $J = 3/2$ atomic states with $J_z = +3/2$ (a), $J_z = +1/2$ (b), $J_z = -1/2$ (c), and $J_z = -3/2$ (d). The CrI₃ monolayer is characterized by an upper valence band which is isolated in energy in the central part of the BZ. The corresponding states are predominantly I-5*p* spin-orbital states, with total momentum $J = 3/2$ and component $J_z = 3/2$. Apart from the main $|J = 3/2, J_z = 3/2\rangle$ component, the highest valence band also includes a small, but non-negligible, I-5*p* $|J = 3/2, J_z = -1/2\rangle$ component for k radii $0.2 - 0.3 \cdot 2\pi/a$. The states of the upper valence band have vanishing in-plane $\mathbf{S}_{\parallel}(\mathbf{k})$ in the central part of the BZ, as a result of the rule: $\langle J, J_z | \hat{\sigma}_\alpha | J, J_z' \rangle \neq 0$, $\alpha = x, y$, only when $\Delta J_z = \pm 1$. We also denote, in Fig. A2, the bands which interact through the Rashba term, see Section VIII.1. We note that the monolayer $J_z = +1/2$ states with p_z component move higher in energy upon formation of the bilayer.[51]

A2. CrI₃ FM bilayer: spin texture of second-highest valence band

Figure A3 shows the in-plane spin texture plot for the second highest valence band of the pristine FM bilayer. Comparing to the spin texture plot of the highest valence band, in Fig. A3, one sees that the in-plane spin polarization components of the first and second highest valence states are opposite in the regions of the six spin patches.

A3. Implications of magnetic group symmetries on spin textures and related quantities

To establish in general the symmetry properties of the spin texture and spin-polarization density in momentum space, considering the magnetic group of a given magnetic system, we distinguish between operators involving time reversal and those which do not involve time reversal. We consider non-degenerate states (as normally is the case in a FM system) at \mathbf{k} points around Γ , i.e., with \mathbf{k} relative to the BZ center. For degenerate states, the same result on symmetries applies to the generalized quantity obtained by summing over the degenerate states.

For an operator that does not involve time reversal, i.e., a spatial symmetry operation, $\{R|\mathbf{f}\}$, where R is a point-group operation and \mathbf{f} a fractional translation, the fact that $\{R|\mathbf{f}\}$ commutes with H_{KS} implies for the energy eigenvalues: $E_n(R\mathbf{k}) = E_n(\mathbf{k})$. Furthermore, for the non-degenerate eigenstates at \mathbf{k} , it implies for the corresponding probability densities: $|\psi_{n,R\mathbf{k}}|^2(\mathbf{r}) = |\psi_{n,\mathbf{k}}|^2(R^{-1}\mathbf{r} - R^{-1}\mathbf{f})$, for the spin-polarization densities: $\mathbf{m}^{(n,R\mathbf{k})}(\mathbf{r}) = \{R|\mathbf{f}\}\mathbf{m}^{(n,\mathbf{k})}(\mathbf{r})$, and for the spin expectation values: $\mathbf{S}(n, R\mathbf{k}) = R\mathbf{S}(n, \mathbf{k})$.

Time reversal is acting on spinors as:[62] $T\psi_{(n,\mathbf{k})}(\mathbf{r}) = i\hat{\sigma}_y\psi_{n,\mathbf{k}}^*(\mathbf{r})$. Taking this into account, and considering then a spatial operator $\{R'|\mathbf{f}'\}T$ of the magnetic point group, with R' a spatial point-group symmetry operation and \mathbf{f}' a fractional translation, the commutativity of $\{R'|\mathbf{f}'\}T$ with H_{KS} implies for the energy eigenvalues: $E_n(-R'\mathbf{k}) = E_n(\mathbf{k})$. For the non-degenerate eigenstates at \mathbf{k} , it implies for the associated probability densities: $|\psi_{n,-R'\mathbf{k}}|^2(\mathbf{r}) = |\psi_{n,\mathbf{k}}|^2(R'^{-1}\mathbf{r} - R'^{-1}\mathbf{f}')$, for the spin-polarization densities: $\mathbf{m}^{(n,-R'\mathbf{k})}(\mathbf{r}) = \{R'|\mathbf{f}'\}T\mathbf{m}^{(n,\mathbf{k})}(\mathbf{r})$, and for the spin expectation values: $\mathbf{S}(n, -R'\mathbf{k}) = R'T\mathbf{S}(n, \mathbf{k})$.

The spin expectation values, \mathbf{S} , and the spin-polarization density, \mathbf{m} , are axial vectors (vectors with a virtual current loop), and transform accordingly under time reversal (i.e., $T\mathbf{S} = -\mathbf{S}$ and $T\mathbf{m} = -\mathbf{m}$) and under spatial operations R, R' [63] Using this and the above relations for \mathbf{S} and \mathbf{m} , with the operators of the magnetic group of the system under consideration, yields the correspondence rules for \mathbf{S} and \mathbf{m} at \mathbf{k} points related by the symmetry operators. In the specific case of the $C_{2h}[C_i]$ magnetic point group, this yields the correspondence rules given in Table I.

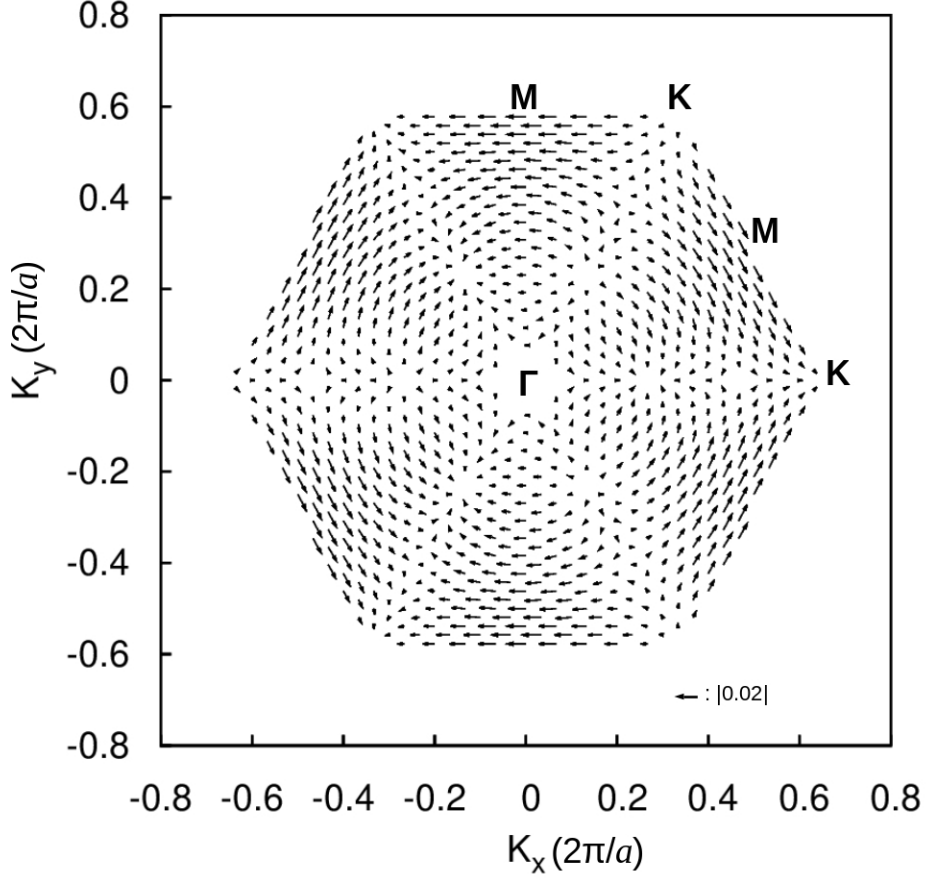


FIG. A1. In-plane spin texture for the highest valence band of the CrI₃ FM monolayer in the 2D BZ.

A4. Effect of \mathcal{E}_z on the monolayer highest valence states

We are interested in the perturbation effect of the Rashba term H_R^L (or H_R) on the states of the monolayer highest-valence band in the central part of the BZ, i.e., with $J_z = +3/2$. We work at fixed \mathbf{k} and consider \mathbf{k} along the k_x axis. The four highest valence states of the monolayer at and near Γ correspond essentially to the four different I-5p $J = 3/2$ atomic spin-orbital states on the Iodine atoms with $J_z = \pm 3/2$ and $\pm 1/2$ (see Fig. A2), where the z axis is along the spins of the Cr atoms (see Fig.1). The Rashba term H_R^L (or H_R) couples only onsite states with $\Delta J_z = \pm 1$. Hence, the highest valence state with $J_z = +3/2$ couples via H_R^L only to the $J_z = +1/2$ state of the same monolayer. In Fig. 7(a), for layer 1, the $J_z = +3/2$ state is $|A\rangle$ and the $J_z = +1/2$ state is $|B\rangle$, and the Rashba coupling is given by $\langle A|H_R^L|B\rangle = \langle B|H_R^L|A\rangle^* \neq 0$.

As the difference between the two energy levels, $E_A - E_B$, is significantly larger than the magnitude of their coupling $|\langle A|H_R^L|B\rangle|$, the Löwdin approach is used to include the correction induced by $\langle B|H_R^L|A\rangle$ to the diagonal matrix element of the Hamiltonian of the highest valence state $|A\rangle$ on layer 1: $\Delta E = \frac{|\langle A|H_R^L|B\rangle|^2}{E - E_B}$, where $E \approx E_A$.

The same holds for $|A'\rangle$ and $|B'\rangle$ on layer 2. The Rashba term H_R^L for layer 2, however, has the opposite sign relative to layer 1, due to the opposite local electric field. Taking this into account and considering also the coupling $\langle A|\Delta V|A'\rangle$ between states of the two layers, the Löwdin-corrected bonding and antibonding type states are proportional to: $|A\rangle + \chi|B\rangle \pm (|A'\rangle - \chi|B'\rangle)$, with $\chi = \frac{\langle B|H_R^L|A\rangle}{E - E_B}$. Using for $|A\rangle$ and $|B\rangle$, the spin-orbital states $|J_z = 3/2\rangle$ and $|J_z = 1/2\rangle$ given in the SI, χ is found to be purely imaginary ($\chi = i\alpha$, with α real), and involves coupling between p_x orbital on one layer and p_z orbital on the other layer. For \mathbf{k} along the k_x axis the corresponding in-plane spin-polarization components for the “bonding” and “antibonding” states on the two layers are along the y axis, and are opposite on the two layers (and same for the two states).

A4.1. Effect of the interlayer chiral potential on the highest valence states

We have seen in Section VII that the interlayer chiral potential $\Delta V(\mathbf{r})$ is responsible for the in-plane spin texture. Furthermore, we have seen, in Section V, that for the upper valence states the in-plane spin texture

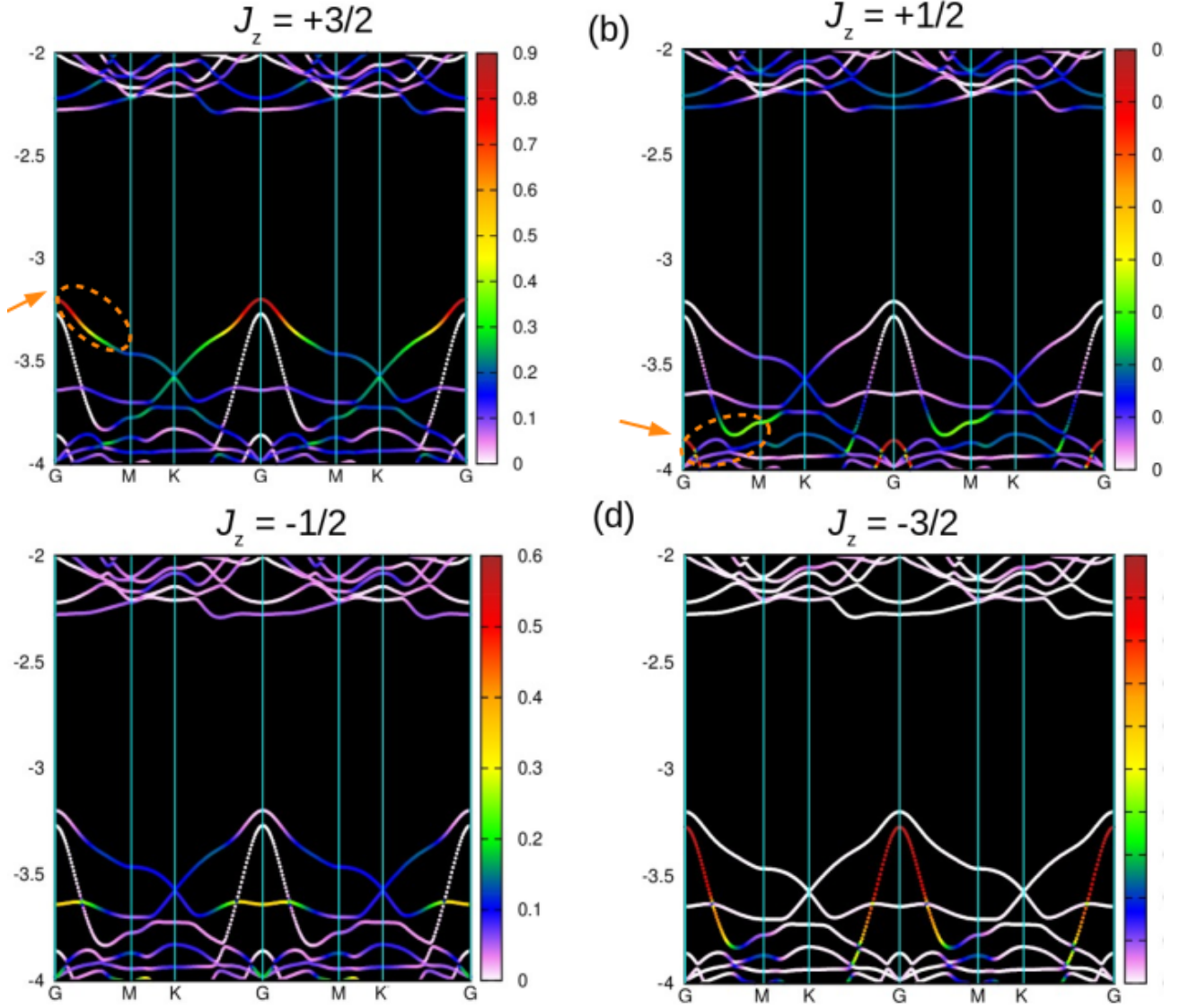


FIG. A2. The same as in Fig. 6, but for the CrI₃ monolayer. The bands interacting through the Rashba term are denoted by the orange ellipses in (a) and (b) - *e.g.* the first and fourth band at Γ .

requires coupling between the $J_z = 3/2$ and $J_z = 1/2$ states. Here we examine which type of coupling between such states (intralayer versus interlayer) can explain the main behavior of the spin-polarization density observed, in Section V, for the two upper valence states with \mathbf{k} along the k_x axis (in the spin patch).

We consider first the interlayer coupling between $|J_z = +3/2\rangle$ and $|J_z = +1/2\rangle$ states induced by ΔV , i.e., the $\langle A|\Delta V|B'\rangle = \langle B'|\Delta V|A\rangle^*$ and $\langle A'|\Delta V|B\rangle = \langle B|\Delta V|A'\rangle^*$ matrix elements. As in the Rashba case, the difference between the energy levels, $E_A - E_B$, is large compared to the magnitude of these matrix elements, whose effect on the upper valence states is treated within the Löwdin perturbation approach. The corresponding correction to the diagonal matrix element for the highest valence state $|A\rangle$ on layer 1 is given by: $\Delta E = \frac{|\langle B'|\Delta V|A\rangle|^2}{E - E_{B'}}$, with $E \approx E_A$. The same holds

for layer 2. As ΔV is inversion symmetric, one has $\langle A|\Delta V|B'\rangle = \langle A'|\Delta V|B\rangle$. Taking this into account and considering also the interlayer coupling $\langle A|\Delta V|A'\rangle$, the corresponding Löwdin-corrected bonding and antibonding type states are proportional to: $|A\rangle + \beta|B'\rangle \pm (|A'\rangle + \beta|B\rangle)$, with $\beta = \frac{\langle B'|\Delta V|A\rangle}{E - E_{B'}}$. Using for $|A\rangle$ and $|B'\rangle$, the spin-orbital states $|J_z = 3/2\rangle$ on layer 1 and $|J_z = 1/2\rangle$ on layer 2 of the SI for \mathbf{k} along the k_x axis, and $E \approx E_A$, the corresponding bonding and antibonding states yield in-plane spin-polarization components, m_x , which are the same on the two layers, and opposite for the two states. This is consistent with the behavior observed for the two highest valence states of the bilayer in Section V.

Considering, instead, as main A - B type of coupling the intralayer coupling $\langle A|\Delta V|B\rangle$ and $\langle A'|\Delta V|B'\rangle$, the corresponding Löwdin-corrected bonding and antibonding type states would be proportional to: $|A\rangle + \beta'|B\rangle \pm (|A'\rangle +$

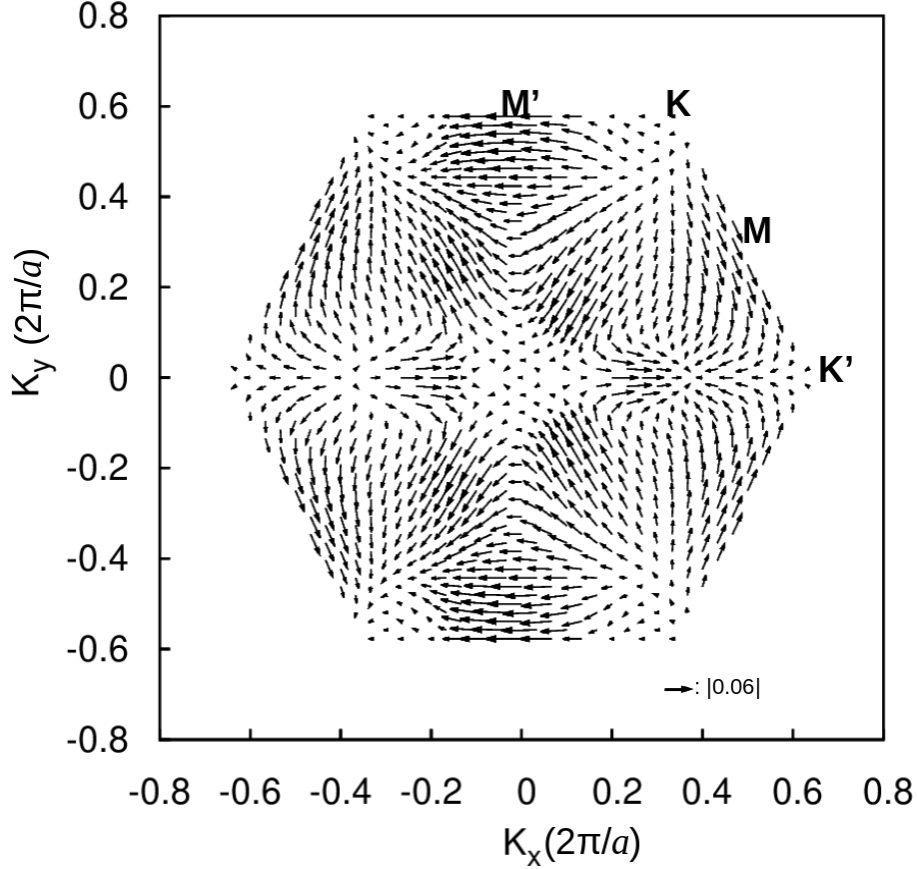


FIG. A3. In-plane spin texture for the second highest valence band of the CrI₃ FM bilayer.

$\beta'|B'\rangle$), with $\beta' = \frac{\langle B|\Delta V|A\rangle}{E-E_B}$. These states yield m_x spin-polarization components which are the same for the two states, and would therefore not account for the spin-polarization behavior for the upper two valence states

obtained from the *ab initio* calculations. Hence, it is the coupling induced by ΔV between $J_z = 3/2$ and $J_z = 1/2$ states of different layers which controls the trends observed in the in-plane spin texture.

-
- [1] A. Manchon, H. C. Koo, J. Nitta, S. M. Frolov, and R. A. Duine, New perspectives for rashba spin-orbit coupling, *Nat. Mater.* **14**, 871 (2015).
- [2] A. Soumyanarayanan, N. Reyren, A. Fert, and C. Panagopoulos, Emergent phenomena induced by spin-orbit coupling at surfaces and interfaces, *Nature* **539**, 509 (2016).
- [3] A. Manchon, J. Zelezny, I. M. Miron, T. Jungwirth, J. Sinova, A. Thiaville, K. Garello, and P. Gambardella, Current-induced spin-orbit torques in ferromagnetic and antiferromagnetic systems, *Rev. Mod. Phys.* **91**, 035004 (2019).
- [4] J. Schliemann, Persistent spin textures in semiconductor nanostructures, *Rev. Mod. Phys.* **89**, 011001 (2017).
- [5] L. L. Tao and E. Y. Tsymlal, Persistent spin texture enforced by symmetry, *Nat. Commun.* **9**, 2763 (2018).
- [6] L. L. Tao, T. R. Paudel, A. A. Kovalev, and E. Y. Tsymlal, Reversible spin texture in ferroelectric HfO₂, *Phys. Rev. B* **95**, 245141 (2017).
- [7] X. Zhang, J.-X. Shen, and C. G. Van de Walle, Three-dimensional spin texture in hybrid perovskites and its impact on optical transitions, *J. Phys. Chem. Lett.* **9**, 2903 (2018).
- [8] M. Sakano, M. Hirayama, T. Takahashi, S. Akebi, M. Nakayama, K. Kuroda, K. Taguchi, T. Yoshikawa, K. Miyamoto, T. Okuda, K. Ono, H. Kumigashira, T. Ideue, Y. Iwasa, N. Mitsuishi, K. Ishizaka, S. Shin, T. Miyake, S. Murakami, T. Sasagawa, and T. Kondo, Radial spin texture in elemental tellurium with chiral crystal structure, *Phys. Rev. Lett.* **124**, 136404 (2020).
- [9] Z. Liu, S. Thirupathaiah, A. N. Yaresko, S. Kushwaha, Q. Gibson, W. Xia, Y. Guo, D. Shen, R. J. Cava, and S. V. Borisenko, A giant bulk-type dresselhaus splitting with 3D chiral spin texture in IrBiSe, *Phys. Status Solidi (RRL)* **14**, 1900684 (2020).
- [10] K. Zollner, M. D. Petrović, K. Dolui, P. Plecháč, B. K. Nikolić, and J. Fabian, Scattering-induced and highly tunable by gate damping-like spin-orbit torque in graphene doubly proximitized by two-dimensional magnet Cr₂Ge₂Te₆ and monolayer WS₂, *Phys. Rev. Research*

- 2**, 043057 (2020).
- [11] Y. Q. Huang, I. A. Buyanova, and W. M. Chen, Scattering symmetry-breaking induced spin photocurrent from out-of-plane spin texture in a 3D topological insulator, *Sci. Rep.* **10**, 10610 (2020).
- [12] H. J. Zhao, H. Nakamura, R. Arras, C. Paillard, P. Chen, J. Gosteau, X. Li, Y. Yang, and L. Bellaiche, Purely cubic spin splittings with persistent spin textures, *Phys. Rev. Lett.* **125**, 216405 (2020).
- [13] K. Yananose, G. Cantele, P. Lucignano, S.-W. Cheong, J. Yu, and A. Stroppa, Chirality-induced spin texture switching in twisted bilayer graphene, *Phys. Rev. B* **104**, 075407 (2021).
- [14] C. M. Acosta, G. M. Dalpian, and A. Zunger, Different shapes of spin textures as a journey through the Brillouin zone, *Phys. Rev. B* **104**, 104408 (2021).
- [15] X. Zhang, Q. Liu, J.-W. Luo, A. J. Freeman, and A. Zunger, Hidden spin polarization in inversion-symmetric bulk crystals, *Nat. Phys.* **10**, 387 (2014).
- [16] L. Yuan, Q. Liu, X. Zhang, J.-W. Luo, S.-S. Li, and A. Zunger, Uncovering and tailoring hidden Rashba spin-orbit splitting in centrosymmetric crystal, *Nature Commun.* **10**, 906 (2019).
- [17] W. Yao, E. Wang, H. Huang, K. Deng, M. Yan, K. Zhang, K. Miyamoto, T. Okuda, L. Li, Y. Wang, H. Gao, C. Liu, W. Duan, and S. Zhou, Direct observation of spin-layer locking by local Rashba effect in monolayer semiconducting PtSe₂ film, *Nature Commun.* **8**, 14216 (2017).
- [18] C. Gong, L. Li, Z. Li, H. Ji, A. Stern, Y. Xia, T. Cao, W. Bao, C. Wang, Y. Wang, Z. Q. Qiu, R. J. Cava, S. G. Louie, J. Xia, and X. Zhang, Discovery of intrinsic ferromagnetism in two-dimensional van der Waals crystals, *Nature* **546**, 265 (2017).
- [19] B. Huang, G. Clark, E. Navarro-Moratalla, D. R. Klein, R. Cheng, K. L. Seyler, D. Zhong, E. Schmidgall, M. A. McGuire, D. H. Cobden, W. Yao, D. Xiao, P. Jarillo-Herrero, and X. Xu, Layer-dependent ferromagnetism in a van der Waals crystal down to the monolayer limit, *Nature* **546**, 270 (2017).
- [20] K. S. Burch, D. Mandrus, and J.-G. Park, Magnetism in two-dimensional van der Waals materials, *Nature* **563**, 47 (2018).
- [21] M. Gibertini, M. Koperski, A. F. Morpurgo, and K. S. Novoselov, Magnetic 2D materials and heterostructures, *Nat. Nanotechnol.* **14**, 408 (2019).
- [22] D. Soriano, M. I. Katsnelson, and J. Fernandez-Rossier, Magnetic two-dimensional chromium trihalides: a theoretical perspective, *Nano Lett.* **20**, 6225 (2020).
- [23] W. Chen, Z. Sun, Z. Wang, L. Gu, X. Xu, S. Wu, and C. Gao, Direct observation of van der Waals stacking-dependent interlayer magnetism, *Science* **366**, 983–(2019).
- [24] X. Cai, T. Song, N. P. Wilson, G. Clark, M. He, X. Zhang, T. Taniguchi, K. Watanabe, W. Yao, D. Xiao, M. A. McGuire, D. H. Cobden, and X. Xu, Atomically thin CrCl₃: An in-plane layered antiferromagnetic insulator, *Nano Lett.* **19**, 3993–(2019).
- [25] B. Huang, G. Clark, D. R. Klein, D. MacNeill, E. Navarro-Moratalla, K. L. Seyler, N. Wilson, M. A. McGuire, D. H. Cobden, D. Xiao, W. Yao, P. Jarillo-Herrero, and X. Xu, Electrical control of 2D magnetism in bilayer CrI₃, *Nat. Nanotechnol.* **13**, 544 (2018).
- [26] S. Jiang, J. Shan, and K. F. Mak, Electric-field switching of two-dimensional van der Waals magnets, *Nat. Mater.* **17**, 406 (2018).
- [27] T. Song, Z. Fei, M. Yankowitz, Z. Lin, Q. Jiang, K. Hwangbo, Q. Zhang, B. Sun, T. Taniguchi, K. Watanabe, M. A. McGuire, D. Graf, T. Cao, J.-H. Chu, D. H. Cobden, C. R. Dean, D. Xiao, and X. Xu, Switching 2D magnetic states via pressure tuning of layer stacking, *Nat. Mater.* **18**, 1298 (2019).
- [28] T. Li, S. Jiang, N. Sivadas, Z. Wang, Y. Xu, D. Weber, J. E. Goldberger, K. Watanabe, T. Taniguchi, C. J. Fennie, K. Fai Mak, and J. Shan, Pressure-controlled interlayer magnetism in atomically thin CrI₃, *Nat. Mater.* **18**, 1303 (2019).
- [29] S. Jiang, L. Li, Z. Wang, K. F. Mak, and J. Shan, Controlling magnetism in 2D CrI₃ by electrostatic doping, *Nat. Nanotechnol.* **13**, 549 (2018).
- [30] Z. Wang, T. Zhang, M. Ding, B. Dong, Y. Li, M. Chen, X. Li, J. Huang, H. Wang, X. Zhao, Y. Li, D. Li, C. Jia, L. Sun, H. Guo, Y. Ye, D. Sun, Y. Chen, T. Yang, J. Zhang, S. Ono, Z. Han, and Z. Zhang, Electric-field control of magnetism in a few-layered van der Waals ferromagnetic semiconductor, *Nat. Nanotechnol.* **13**, 554 (2018).
- [31] I. A. Verzhbitskiy, H. Kurebayashi, H. Cheng, J. Zhou, S. Khan, Y. P. Feng, and G. Eda, Controlling the magnetic anisotropy in Cr₂Ge₂Te₆ by electrostatic gating, *Nat. Electronics* **3**, 460 (2020).
- [32] T. Song, X. Cai, M. W.-Y. Tu, X. Zhang, B. Huang, N. P. Wilson, K. L. Seyler, L. Zhu, T. Taniguchi, K. Watanabe, M. A. McGuire, D. H. Cobden, D. Xiao, W. Yao, and X. Xu, Giant tunneling magnetoresistance in spin-filter van der Waals heterostructures, *Science* **360**, 1214 (2018).
- [33] C. Cardoso, D. Soriano, N. A. Garcá-Martínez, and J. Fernández-Rossier, Van der Waals spin valves, *Phys. Rev. Lett.* **121**, 067701 (2018).
- [34] D. R. Klein, D. MacNeill, J. L. Lado, D. Soriano, E. Navarro-Moratalla, K. Watanabe, T. Taniguchi, S. Manni, P. Canfield, J. Fernández-Rossier, and P. Jarillo-Herrero, Probing magnetism in 2D van der Waals crystalline insulators via electron tunneling, *Science* **360**, 1218 (2018).
- [35] Z. Wang, I. Gutiérrez-Lezama, N. Ubrig, M. Kroner, M. Gibertini, T. Taniguchi, K. Watanabe, A. Imamoğlu, E. Giannini, and A. F. Morpurgo, Very large tunneling magnetoresistance in layered magnetic semiconductor CrI₃, *Nat. Commun.* **9**, 2516 (2018).
- [36] K. Dolui, M. D. Petrović, K. Zollner, P. Plecháč, J. Fabian, and B. K. Nikolić, Proximity spin-orbit torque on a two-dimensional magnet within van der Waals heterostructure: Current-driven antiferromagnet-to-ferromagnet reversible nonequilibrium phase transition in bilayer CrI₃, *Nano Lett.* **20**, 2288 (2020).
- [37] K. Yang, W. Hu, H. Wu, M.-H. Whangbo, P. G. Radaelli, and A. Stroppa, Magneto-optical Kerr switching properties of (CrI₃)₂ and (CrBr₃/CrI₃) bilayers, *ACS Appl. Electron. Mater.* **2**, 1373 (2020).
- [38] Y. Zhang, T. Holder, H. Ishizuka, F. de Juan, N. Nagaosa, C. Felser, and B. Yan, Switchable magnetic bulk photovoltaic effect in the two-dimensional magnet CrI₃, *Nat. Commun.* **10**, 3783 (2019).
- [39] X. Cheng, Z. Cheng, C. Wang, M. Li, P. Gu, S. Yang, Y. Li, K. Watanabe, T. Taniguchi, W. Ji, and L. Dai, Light helicity detector based on 2D magnetic semiconductor CrI₃, *Nat. Commun.* **12**, 6874 (2021).
- [40] K. Yamauchi, P. Barone, and S. Picozzi, Bulk Rashba effect in multiferroics: A theoretical prediction for BiCoO₃,

- Phys. Rev. B **100**, 245115 (2019).
- [41] F. Lou, T. Gu, J. Ji, J. Feng, H. Xiang, and A. Stroppa, Tunable spin textures in polar antiferromagnetic hybrid organic–inorganic perovskites by electric and magnetic fields, *npj Comput. Mater.* **6**, 114 (2020).
- [42] L. Yuan, Z. Wang, J. Luo, E. Rashba, and A. Zunger, Giant momentum-dependent spin splitting in centrosymmetric low- antiferromagnets, *Phys. Rev. B* **102**, 014422 (2020).
- [43] S. Ghosh, N. Stojić, and N. Binggeli, Rashba-induced spin texture and spin-layer-locking effects in antiferromagnetic CrI₃ bilayer, (2022), arXiv:2202.09431 [cond-mat.mtrl-sci].
- [44] O. Krupin, G. Bihlmayer, K. Starke, S. Gorovikov, J. E. Prieto, K. Döbrich, S. Blügel, and G. Kaindl, Rashba effect at magnetic metal surfaces, *Phys. Rev. B* **71**, 201403(R) (2005).
- [45] J. Zhang, J. P. Velev, X. Dang, and E. Y. Tsymbal, Band structure and spin texture of Bi₂Se₃ 3d ferromagnetic metal interface, *Phys. Rev. B* **94**, 014435 (2016).
- [46] G. Margalit, B. Yan, and Y. Oreg, Induced half-metallicity and gapless chiral topological superconductivity in the CrI₃–Pb interface, *Phys. Rev. B* **102**, 024515 (2020).
- [47] Z. Sun, Y. Yi, T. Song, G. Clark, B. Huang, Y. Shan, S. Wu, D. Huang, C. Gao, Z. Chen, M. McGuire, T. Cao, D. Xiao, W.-T. Liu, W. Yao, X. Xu, and S. Wu, Giant nonreciprocal second-harmonic generation from antiferromagnetic bilayer CrI₃, *Nature* **572**, 497 (2019).
- [48] N. Sivadas, S. Okamoto, X. Xu, C. J. Fennie, and D. Xiao, Stacking-dependent magnetism in bilayer CrI₃, *Nano Lett.* **18**, 7658 (2018).
- [49] P. Jiang, C. Wang, D. Chen, Z. Zhong, Z. Yuan, Z.-Y. Lu, and W. Ji, Stacking tunable interlayer magnetism in bilayer CrI₃, *Phys. Rev. B* **99**, 144401 (2019).
- [50] D. Soriano, C. Cardoso, and J. Fernández-Rossier, Interplay between interlayer exchange and stacking in CrI₃ bilayers, *Solid State Communications* **299**, 113662 (2019).
- [51] S. Ghosh, N. Stojić, and N. Binggeli, Overcoming the asymmetry of the electron and hole doping for magnetic transitions in bilayer CrI₃, *Nanoscale* **13**, 9391 (2021).
- [52] J. L. Lado and J. Fernández-Rossier, On the origin of magnetic anisotropy in two dimensional CrI₃, *2D Mater.* **4**, 035002 (2017).
- [53] M. A. McGuire, H. Dixit, V. R. Cooper, and B. C. Sales, Coupling of crystal structure and magnetism in the layered, ferromagnetic insulator CrI₃, *Chem. Mater.* **27**, 612 (2015).
- [54] N. Ubrig, Z. Wang, J. Teyssier, T. Taniguchi, K. Watanabe, E. Giannini, A. F. Morpurgo, and M. Gibertini, Low-temperature monoclinic layer stacking in atomically thin CrI₃ crystals, *2D Mater.* **7**, 015007 (2019).
- [55] M. Gibertini, Magnetism and stability of all primitive stacking patterns in bilayer chromium trihalides, *J. Phys. D: Appl. Phys.* **54**, 064002 (2020).
- [56] P. Giannozzi, S. Baroni, N. Bonini, M. Calandra, R. Car, C. Cavazzoni, D. Ceresoli, G. L. Chiarotti, M. Cococcioni, I. Dabo, A. D. Corso, S. de Gironcoli, S. Fabris, G. Fratesi, R. Gebauer, U. Gerstmann, C. Gougoussis, A. Kokalj, M. Lazzeri, L. Martin-Samos, N. Marzari, F. Mauri, R. Mazzarello, S. Paolini, A. Pasquarello, L. Paulatto, C. Sbraccia, S. Scandolo, G. Sclauzero, A. P. Seitsonen, A. Smogunov, P. Umari, and R. M. Wentzcovitch, *J. Condens. Matter Phys.* **21**, 395502 (2009).
- [57] J. P. Perdew and A. Zunger, Self-interaction correction to density-functional approximations for many-electron systems, *Phys. Rev. B* **23**, 5048 (1981).
- [58] D. M. Ceperley and B. J. Alder, Ground state of the electron gas by a stochastic method, *Phys. Rev. Lett.* **45**, 566 (1980).
- [59] E. Kucukbenli, M. Monni, B. I. Adetunji, X. Ge, G. A. Adebayo, N. Marzari, S. de Gironcoli, and A. D. Corso, Projector augmented-wave and all-electron calculations across the periodic table: a comparison of structural and energetic properties (2014), arXiv:1404.3015 [cond-mat.mtrl-sci].
- [60] P. E. Blöchl, Projector augmented-wave method, *Phys. Rev. B* **50**, 17953 (1994).
- [61] A. M. León, J. W. González, J. Mejía-López, F. C. de Lima, and E. S. Morell, Strain-induced phase transition in CrI₃ bilayers, *2D Materials* **7**, 035008 (2020).
- [62] F. Bassani and G. Pastori Parravicini, *Electronic States and Optical Transitions in Solids* (Pergamon Press, 1975).
- [63] L. C. Chapon, An introduction to the use of representation analysis for studying magnetoelectrics and multiferroics, *EPJ Web of Conferences* **22**, 00013 (2012).
- [64] S. R. Park, C. H. Kim, J. Yu, J. H. Han, and C. Kim, Orbital-angular-momentum based origin of rashba-type surface band splitting, *Phys. Rev. Lett.* **107**, 156803 (2011).

TABLE I. Symmetry operators of the magnetic point group of the CrI₃ FM bilayer and correspondence rules for the probability density, spin-polarization density, and spin expectation values at \mathbf{k} points related by the symmetry operators. The reference probability-density function $|\psi|^2(\mathbf{r})$, spin-polarization-density functions $m_x(\mathbf{r})$, $m_y(\mathbf{r})$, $m_z(\mathbf{r})$, and spin expectation values S_x , S_y , S_z are those of a non-degenerate eigenstate at a point (k_x, k_y) in the BZ. The position \mathbf{r} is relative to an inversion symmetry point of the bilayer, and \mathbf{k} is relative to the BZ center.

Symmetry	\mathbf{k}	$ \Psi_{\mathbf{k}} ^2$	$\mathbf{m}_{\mathbf{k}}$	$\mathbf{S}_{\mathbf{k}}$
E	k_x, k_y	$ \Psi ^2(x, y, z)$	$m_x(x, y, z), m_y(x, y, z), m_z(x, y, z)$	S_x, S_y, S_z
I	$-k_x, -k_y$	$ \Psi ^2(-x, -y, -z)$	$m_x(-x, -y, -z), m_y(-x, -y, -z), m_z(-x, -y, -z)$	S_x, S_y, S_z
$R_y(180^\circ) \cdot T$	$k_x, -k_y$	$ \Psi ^2(-x, y, -z)$	$m_x(-x, y, -z), -m_y(-x, y, -z), m_z(-x, y, -z)$	$S_x, -S_y, S_z$
$M_{xz} \cdot T$	$-k_x, k_y$	$ \Psi ^2(x, -y, z)$	$m_x(x, -y, z), -m_y(x, -y, z), m_z(x, -y, z)$	$S_x, -S_y, S_z$